


Jet-mode feedback in NGC 5972: insights from resolved MUSE, GMRT and VLA observations

ARSHI ALI,^{1,*} BINY SEBASTIAN,² DARSHAN KAKKAD,³ SILPA SASIKUMAR,⁴ PREETI KHARB,⁵ CHRISTOPHER P. O'DEA,^{2,6}
MAINAK SINGHA,⁷ K RUBINUR ,⁸ STEFI A. BAUM,^{2,6} OMKAR BAIT,⁹ SRAVANI VADDI,¹⁰ AND SUSHMA KURAPATI¹¹

¹*Department of Physics, Savitribai Phule Pune University, Pune 411007, India*

²*Department of Physics and Astronomy, University of Manitoba, Winnipeg, MB R3T 2N2, Canada*

³*Space Telescope Science Institute, 3700 San Martin Drive, Baltimore, MD 21218, USA*

⁴*Departamento de Astronomía, Universidad de Concepción, Concepción, Chile*

⁵*National Centre for Radio Astrophysics (NCRA) - Tata Institute of Fundamental Research (TIFR),
S. P. Pune University Campus, Post Bag 3, Ganeshkhind, Pune 411007, India*

⁶*Center for Space Plasma & Aeronomic Research, University of Alabama in Huntsville, Huntsville, AL 35899 USA*

⁷*Astrophysics Science Division, NASA Goddard Space Flight Center, Greenbelt, MD 20771, USA*

⁸*Institute of Theoretical Astrophysics, University of Oslo, P.O. Box 1029, Blindern, 0315 Oslo, Norway*

⁹*Observatoire de Genève, Université de Genève, Chemin Pegasi, 1290 Versoix, Switzerland*

¹⁰*Department of Physics, University of Central Florida, 4111 Libra Drive, Physical Sciences Bldg. 430, Orlando, FL 32816-2385*

¹¹*University of Cape Town, Rondebosch, Cape Town, 7701*

ABSTRACT

We present a comprehensive analysis of the ionized gas in the kpc-scale extended emission line region (EELR) of NGC 5972, a “Voorwerp” galaxy. We have used optical integral field spectroscopy (IFS) observations from the Multi Unit Spectroscopic Explorer (MUSE) at the Very Large Telescope (VLT) to study the stellar and ionized gas kinematics of the galaxy. We complemented these observations with low-frequency (610 MHz) observations from the Giant Metrewave Radio Telescope (GMRT) and high-frequency (5 GHz) observations from the Very Large Array (VLA) to study the interactions between the radio jet and the ionized gas.

NGC 5972 features a helical-shaped EELR with radius > 10 kpc and a prominent S-shaped radio structure spanning about 550 kpc. Shock modeling and BPT analysis show shock+precursor emissions in the region where [O III] emission overlaps with the radio jet, and pure shock emissions perpendicular to the jet, suggesting jet-induced shocks. We find a spatial correlation between the outflowing gas (in [O III] and H α) and the jet, further supporting the idea of jet feedback. Radio observations indicate episodic AGN activity characterized by surface brightness and spectral index discontinuities. Overall, based on our findings, we propose a jet-driven feedback mechanism as one of the key factors in the formation of the EELR in NGC 5972.

Keywords: Active galactic nuclei (16), Radio galaxies (1343), Radio jets (1347), Spectroscopy (1558), Polarimetry (1278)

1. INTRODUCTION

Understanding AGN feedback is essential because it has become a crucial ingredient in the current cosmological simulations exploring galaxy evolution like IllustrisTNG (Springel et al. 2018; Pillepich et al. 2018; Nelson et al. 2018; Vogelsberger et al. 2018), Horizon-AGN or NewHorizon (Kaviraj et al. 2017; Dubois et al. 2021), EAGLE (Crain et al. 2015; Schaye et al. 2015) and SIMBA (Davé et al. 2019), primarily because of

its role in regulating the star formation rate and determining the efficiency of energy and momentum transfer within the host galaxy. However, this task has often proven to be challenging due to the intricate interplay of various physical processes such as the coexistence of multiple feedback mechanisms, the inherent variability of AGN, the complexity of galactic gas dynamics, limitations of current observational tools and methods, etc. Addressing these challenges is essential for gaining a more comprehensive understanding of how AGN shape the evolution of galaxies.

* E-mail: arshiali1701@gmail.com

Recent studies (Jarvis et al. 2021; Venturi et al. 2021, 2023a; Silpa et al. 2022; Girdhar 2022) find that a large fraction of radio-quiet quasars with kpc-scale ionized outflows show small-scale radio jets, and the gas exhibits enhanced velocity dispersion in the direction perpendicular to the jet. This suggests that jet-ISM interaction is a major player in AGN feedback. Conversely, it was also found that most of the powerful radio galaxies exhibit EELR that can extend up to hundreds of kpcs (e.g., Baum et al. 1988; McCarthy et al. 1995; Balmaverde et al. 2022). Thus, these EELR provide a unique laboratory to study the origin of the AGN activity as well as the various feedback mechanisms (Schawinski et al. 2010; Keel et al. 2012a; Shih & Stockton 2014; Keel et al. 2015; Sartori et al. 2016; Kozlova et al. 2020).

“Voorwerp” galaxies constitute a distinct category of emission line galaxies, which came to light through the involvement of citizen scientists in the Galaxy Zoo project (Lintott et al. 2009; Józsa et al. 2009; Keel et al. 2011). These galaxies are notable for their green appearance in false color-composite images, indicating the prevalence of robust doubly ionized oxygen lines ([O III] λ 5007, [O III] hereafter). Notably, the emission-line ratios observed in these “Voorwerp” galaxies bear a striking resemblance to those found in the EELR (Chojnowski & Keel 2011; Keel et al. 2012b). These sources are suggested to be examples of quasar ionization echoes from previous episodes of AGN activity (Lintott et al. 2009). The radio imaging of several of these galaxies revealed that the [O III] emission is coincident with radio emission (*viz.*, “Teacup Quasar” (Harrison et al. 2015; Venturi et al. 2023b), Mrk 78 (Whittle & Wilson 2004), NGC 4388 (Sebastian et al. 2020). More recently Smith et al. (2022) uncovered the presence of an old relic radio emission from the “Hanny’s Voorwerp” galaxy, IC2497. They argue that the radio jets play a significant role in shaping the ionization structure within their host galaxies. Similarly, recent study of the Teacup Quasar (Venturi et al. 2023b) also shows that the jet strongly perturbs the host ISM. According to previous studies, the feedback in the Voorwerp galaxies is primarily caused by AGN photoionization (Lintott et al. 2009; Keel et al. 2012b, 2017), however, the presence of a radio jet in these galaxies could prompt a discussion of whether jet also plays a significant role in the feedback.

Since the majority of the “Voorwerp” galaxies are Seyfert galaxies, the origin of the radio emission itself is highly debated. The correlation between [O III] and radio luminosity in Seyfert galaxies has been known for several decades (de Bruyn & Wilson 1978a; Schmitt et al. 2003). Similar spatial coincidences were also seen in radio galaxies (Baum & Heckman 1989). While such

spatial correlations might immediately suggest a jet-related origin, alternate explanations, including shock acceleration due to winds driven by the AGN accretion leading to radio emission has been proposed (e.g., Zakamska & Greene (2014)) to explain such correlations in radio-quiet systems.

In this paper, we investigate the impact of radio jets on the ionized gas morphology and kinematics in NGC 5972, a “Voorwerp” galaxy, using optical IFS observations from MUSE instrument at VLT, low frequency (610 MHz) observations from GMRT, and high frequency (5 GHz) observations from VLA. This paper is organized as described below. In section 3 we present the description of MUSE, GMRT, and VLA observations and data analysis. Section 4 consists of results and in section 5 we discuss their implications. The conclusions are summarized in section 6.

We have assumed $H_0=73 \text{ km s}^{-1}\text{Mpc}^{-1}$, $\Omega_m = 0.27$ and $\Omega_{vac} = 0.73$ in this paper. Spectral index α is defined such that flux density at frequency ν is $S_\nu \propto \nu^\alpha$.

2. TARGET SELECTION

From a sample of 19 Voorwerp galaxies listed in Keel et al. (2012a), NGC 5972 was chosen because of the availability of the science-processed MUSE data cube, and low-redshift ($z=0.02964$) which will enable resolved studies. NGC 5972 is an excellent source to study the AGN feedback via jet as it hosts a kpc scale jet that coincides with the EELR. NGC 5972 is classified as a “radio-loud” galaxy ($L_{1.4}=2 \times 10^{24} \text{ W Hz}^{-1}$). According to the radio-loudness parameter (R) as defined in Kellermann et al. (1989), $R \approx 31$, suggests that the origin of radio emission can be attributed by jets powered by the central engine.

3. OBSERVATIONS AND DATA ANALYSIS

3.1. MUSE

The MUSE (Bacon et al. 2010) is an integral field spectrograph located on VLT. NGC 5972 was observed by the MUSE as part of program 0102.B-0107 (PI: SARTORI) on March 10, 2019. We downloaded the fully reduced and calibrated science data cube from the ESO data archive.¹ Observations of NGC 5972 were conducted in wide-field mode (WFM) with a FoV of $1' \times 1'$, and a pixel scale of $0.2''$. More details regarding the observation and data reduction is discussed in Finlez et al. (2022). MUSE data covers a wavelength range of 4600-9300 Å. However, for our purposes, we have only utilized the range between 4600-8800 Å.

¹ <http://archive.eso.org/>

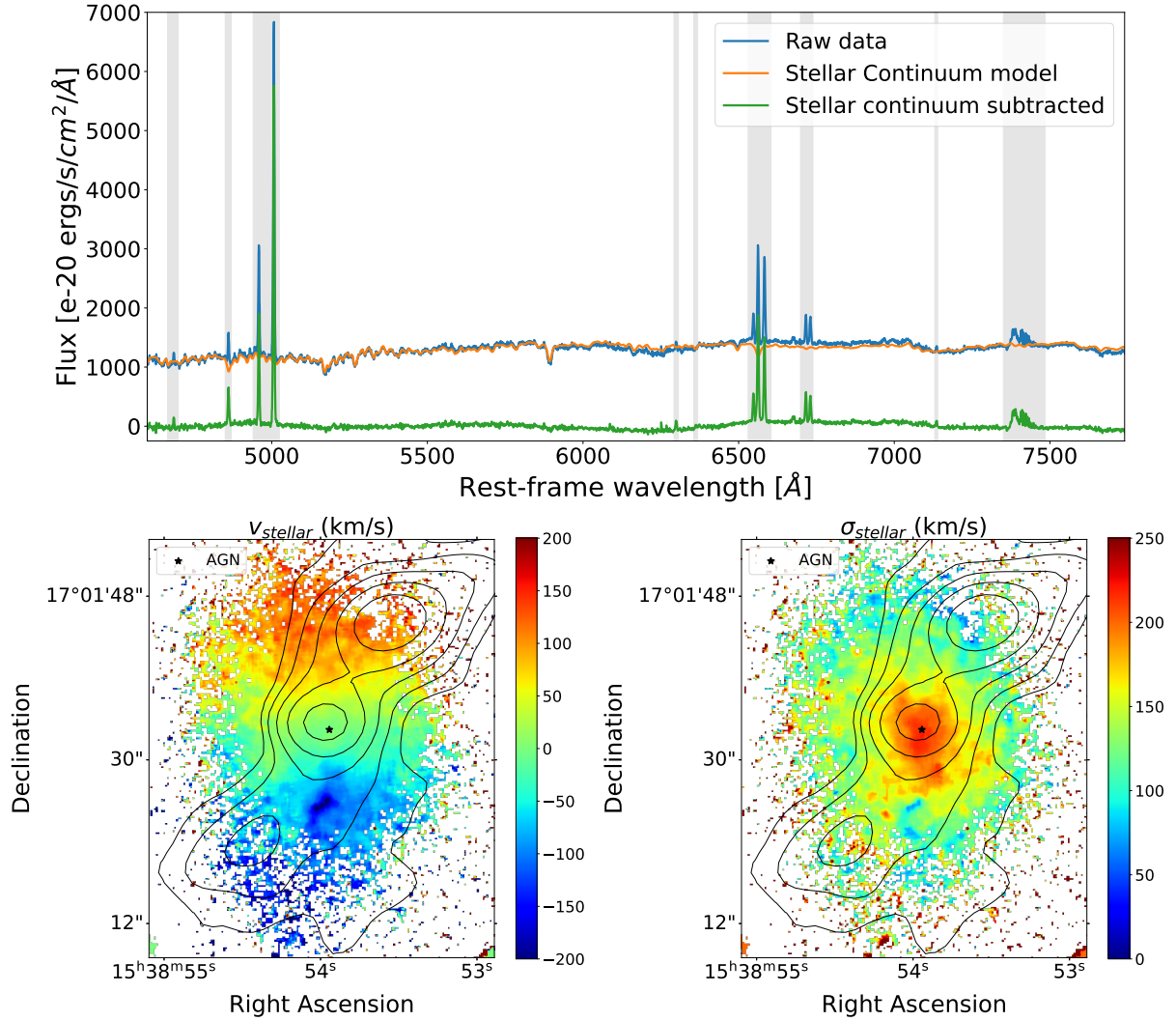


Figure 1. Top: Stellar continuum fit for one of the spaxels of the MUSE data. Excluded sky emission lines are highlighted with shaded regions. Bottom: line-of-sight stellar velocity and stellar dispersion maps obtained after the ppxf fitting. A SNR cut of 3σ was applied, where $\sigma = 5 \text{ km s}^{-1}$ for the stellar dispersion image. The contour corresponds to 610 MHz radio emission with contour levels: $3\sigma \times (1, 2, 4, 8, 16, 32, 64)$, where $\sigma = 98.2 \mu\text{Jy beam}^{-1}$.

To perform the stellar continuum subtraction, we employed the penalized PiXel-Fitting procedure, pPXF (Cappellari & Emsellem 2004; Cappellari 2017) to analyze the entire MUSE FoV ($2.03'$) which encompasses approximately 180,000 spaxels. In order to ensure accurate results, we masked out regions in the spectra that contained strong skylines and emission lines. Specifically, the following lines were masked: He II $\lambda 4685$, H β $\lambda 4861$, O III doublets $\lambda 4958, 5007$, H α $\lambda 6562$, N II doublets $\lambda 6548, 6583$, O I $\lambda 6300$, S II doublets $\lambda 6716, 6730$, and Ar III $\lambda 7135$. Figure 1: top, shows an example of stellar continuum fit for one of the pixels, along with the stellar velocity (bottom left) and stellar dispersion velocity (bottom right) respectively.

We subtracted the modeled stellar continuum emission from the raw data, and the resulting continuum-

subtracted cube was utilized to perform the single or double Gaussian fitting based on the complexity of the line profiles in different regions. We have used the `scipy.curve-fit` Python package (Virtanen et al. 2020) to perform the fitting procedure. The primary objective of this step is to extract the morphological and kinematic information to study the distribution and motion of ionized gas within the host galaxy. We observed that the region within 6 kpc from the nucleus cannot be fitted using only the single Gaussian component, thus we added another Gaussian to account for the additional (outflowing) component. We have primarily used [O III] and H α $\lambda 6562$ emission lines to map the ionized outflowing gas (see detailed discussion in section 5.2.2). After running the fitting procedure once, we intentionally adjusted the widths of Gaussian 1 and Gaussian 2

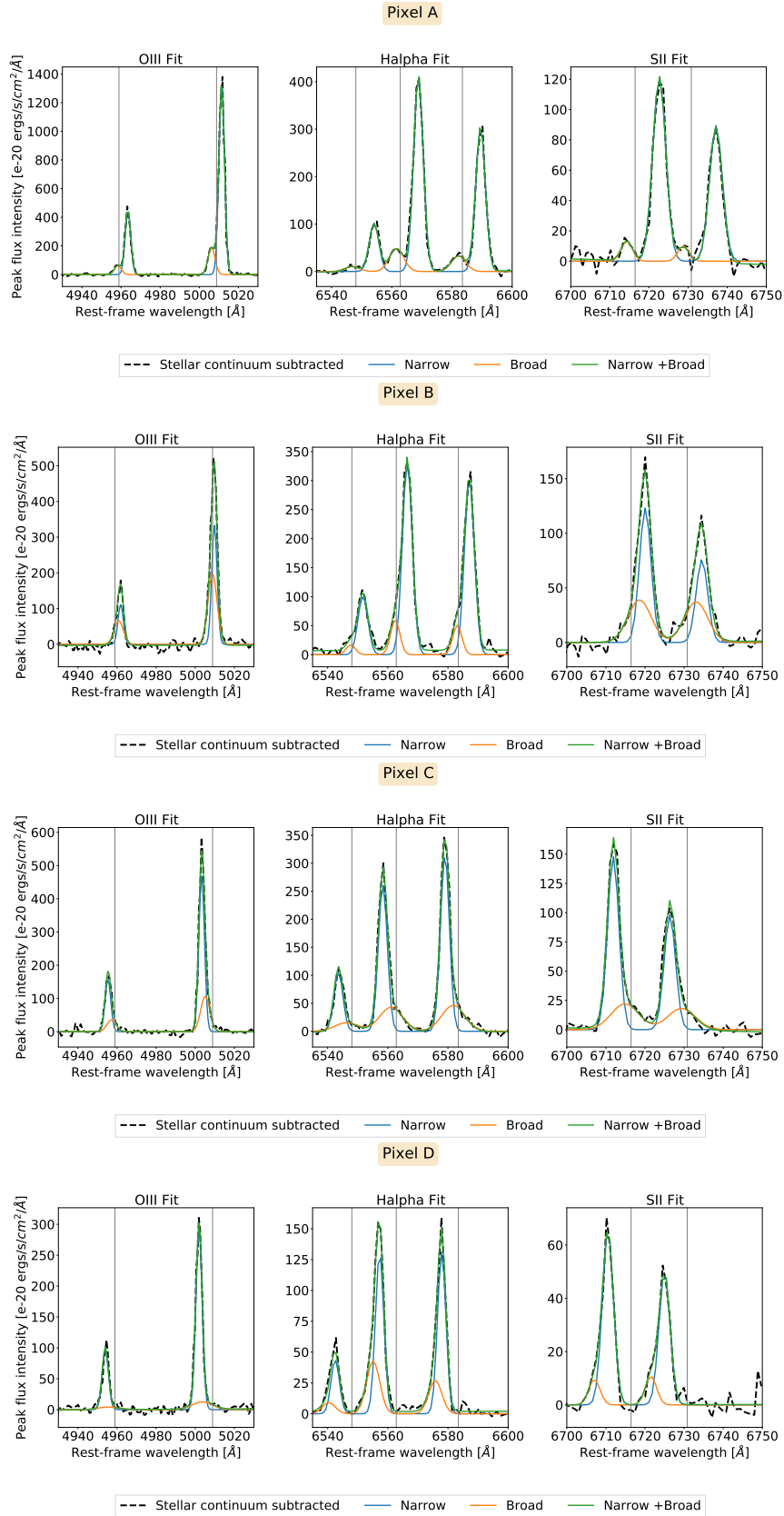
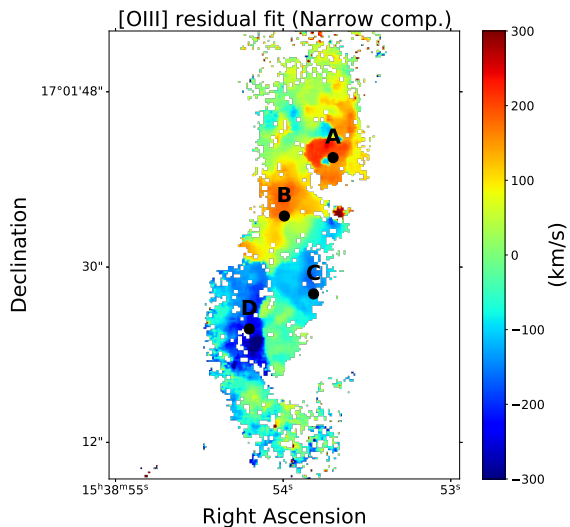


Figure 2. Example of double Gaussian fitting for four distinct locations extracted from the [O III] residual fit for Gaussian 1 component, as shown in Figure 3. Left panels: [O III] $\lambda 4958, 5007$ line profile. Middle panels: H α $\lambda 6562$, N II $\lambda 6548, 6583$ line profile. Right panels: S II $\lambda 6716, 6730$ line profile. In each plot, the stellar continuum subtracted data is represented by the dashed black curve, narrow component (Gaussian 1) by the blue curve, broad component (Gaussian 2) by orange curve, and the narrow+broad (total double Gaussian) by the green curve. Solid grey lines indicate the rest-frame wavelength of the respective emission lines.

Table 1. Details for GMRT and VLA data

GMRT	
Observation Date	2022-05-23
ν (MHz)	610
Beam, PA (arcsec ² , °)	6.5×5.0, 87.97
Image peak flux density (mJy)	6.06
Image r.m.s (mJy beam ⁻¹)	0.075
On source time (min)	150
VLA	
Array Configuration	D
Observation Date	2015-12-13
ν (GHz)	6.0
Beam, PA (arcsec ² , °)	11.3×9.6, 54.11
Image peak flux density (mJy)	4.22
Image r.m.s (mJy beam ⁻¹)	0.034
On source time (min)	35
VLA	
Array Configuration	B
Observation Date	2023-01-14
ν (GHz)	5.5
Beam, PA (arcsec ² , °)	2.43×1.14, 65.03
Image peak flux density (mJy)	4.8
Image r.m.s (mJy beam ⁻¹)	0.008
On source time (min)	60

**Figure 3.** Pixel locations used for representing the double Gaussian fitting in Figure 2. The map used is the [O III] residual fit for Gaussian 1.

by comparing them. Upon this comparison, we swapped the widths to ensure that Gaussian 1 is identified as the narrow component, while Gaussian 2 is referred to as the broad component. The peak intensity of the sec-

ond component is initialized as half the peak intensity of the first component. To guide the fitting process, we introduce certain constraints to the parameters governing the centroids and FWHM of the individual Gaussian components used to model the emission lines. The centroids of the following lines: H β λ 4861, [O III] doublets λ 4958, 5007, H α λ 6562, [N II] doublets λ 6548, 6583, and [S II] doublets λ 6716, 6730 were tied together based on their anticipated positions within the rest-frame spectra. The line fluxes were left unconstrained for all the lines, except for the line ratios [O III] λ 5007/ λ 4958 and [N II] λ 6548/ λ 6583, which were set at 3 as per established theoretical values (Storey & Zeppen 2000; Dimitrijević et al. 2007). Fitting for four distinct locations are shown in Figure 2.

Our BPT maps made using the spaxel-by-spaxel analysis were limited to the high SNR regions (refer to section 4.4). Hence, we opted to transition to Voronoi binning to improve our sensitivity and understand the nature of the weaker emission regions. We have used the Galaxy IFU Spectroscopy Tool², GIST (Bittner et al. 2019) for this step. GIST uses a python-implemented version of pPXF and GANDALF (Sarzi et al. 2006; Falcón-Barroso et al. 2006; Bittner et al. 2019) to provide stellar kinematics and emission-line properties, respectively. The pipeline first creates Voronoi bins of the data cube, such that we get a constant SNR across all bins. Bins with continuum SNR \leq 5 were discarded to reduce the noisy spectra, and a minimum SNR cut of 20 is applied on the emission lines. This process resulted in the division of the galaxy into 2103 Voronoi bins over the galaxy-scale frame. Using these bins, the pipeline then performs a stellar kinematics routine using pPXF. We have used the MILES library (Vazdekis et al. 2015) as a template for stellar population synthesis. The stellar spectrum is subtracted from the observed spectra, and the emission line profiles are fitted using pyGANDALF. The algorithm returns the following list of parameters for each line: flux, amplitude, line-of-sight velocity, and velocity dispersion. For the binning procedure, we have set the wavelength range from 4000 Å - 6800 Å which covers the required range of emission lines used in the BPT analysis.

3.2. VLA

3.2.1. Archival data at 6 GHz and new data at 5 GHz

We used archival VLA (Napier et al. 1983; Perley et al. 2011) data of NGC 5972 at 6 GHz (C-band), which was observed on 13 Dec 2015 (PI: Schawinski, Project Id:

² <https://abittner.gitlab.io/thegistpipeline/>

15B-145). The details of the observations are shown in Table 1. 3C 286 was used for flux density and bandpass calibration, whereas J1608+1029 was used as the phase calibrator. Data reduction and calibration of continuum data were performed with the NRAO Common Astronomy Software Applications package (CASA), version 6.2.1-7, using the calibration and imaging pipeline³. We carried out three rounds of phase-only self-calibration on the data while reducing the ‘solint’ with every iteration.

We observed NGC 5972 using the VLA at 5 GHz in the B-array configuration on 14 Jan 2023 (Project Id: 23A-264, PI: Ali). Details of the observations are shown in Table 1. 3C 286 was used for flux density and bandpass calibration, whereas J1504+1029 was used as the phase calibrator. The continuum data were calibrated and edited using the NRAO CASA calibration and imaging pipeline. We then carried out the manual execution of the polarization calibration steps. The strongly polarized 3C 286 was used as the polarization angle calibrator, while the unpolarized calibrator OQ 208 was used for leakage calibration.

The polarization calibration steps included: (i) manually setting the polarization model for 3C 286 using the CASA task SETJY. Parameters such as the reference frequency, the total intensity value at the reference frequency, the spectral index, and the coefficients of the polynomial expansion of fractional polarization and polarization angle as functions of frequency about the reference frequency were provided to define the model; (ii) solving the cross-hand (RL, LR) delays arising from residual delay differences between the right and left circularly polarized signals. This step was carried out using 3C 286 in the CASA task GAINCAL with `gaintype = KCROSS`; (iii) solving instrumental polarization (‘D-terms’ or antenna leakages) arising from imperfect and non-orthogonal antenna feeds, or cross-talk between the feeds. This step was carried out using OQ 208 in the CASA task POLCAL with `poltype = Df`⁴. Five antennas were found to have very high leakage. Therefore, they were flagged at the beginning of the polarization calibration steps. The final leakages obtained were typically < 15%, and finally, (iv) solving the residual R-L phase difference on the reference antenna. This step was carried out using 3C 286 in the CASA task POLCAL with `poltype = Xf`.

³ <https://science.nrao.edu/facilities/vla/data-processing/pipeline/VIPL>

⁴ The parameter `poltype` is set to `Df + QU` if the polarized calibrator is used for leakage calibration. We did not use 3C 286 for leakage calibration here since we had not acquired multiple scans of 3C 286 to ensure a good parallactic angle coverage.

After applying the calibration solutions to the multi-source data set, we extracted the visibility data for NGC 5972 using the CASA task SPLIT while also averaging the spectral channels to handle the bandwidth smearing effects. We used the multi-term-multifrequency synthesis (MT-MFS; Rau & Cornwell 2011) algorithm in the TCLEAN task in CASA to create the continuum or Stokes I image of NGC 5972. We carried out three rounds of phase-only self-calibration followed by one round of amplitude and phase self-calibration. The last self-calibrated visibility data was imaged for Stokes Q and U using the same input parameters as for the Stokes I image except for a fewer number of iterations and the Stokes parameter.

We combined Stokes Q and U images using the AIPS task COMB with `opcode = POLC` (which corrects for Ricean bias) to create the linear polarized intensity ($P = \sqrt{Q^2 + U^2}$; PPOL) image and with `opcode = POLA` to create the polarization angle ($\chi = 0.5 \tan^{-1}(U/Q)$; PANG) image. We blanked the regions with intensity values less than 3 times the rms noise and with angle errors greater than 10° while making PPOL and PANG images, respectively. We created the fractional polarization (FPOL = P/I) image from the PPOL and Stokes I images using the task COMB with `opcode = DIV`. We blanked the regions with fractional polarization errors >10%.

3.3. GMRT

The GMRT observation for NGC 5972 at 610 MHz (Band-4) was carried out on 23 May 2022 (proposal code: 42.015, PI: Ali). For our observations, we have used 3C 286 (polarized calibrator) as the primary flux calibrator, OQ 208 (unpolarized calibrator) as the polarization leakage calibrator and 1347+122 as the phase calibrator. The data analysis was carried out using the GMRT data analysis pipeline `aipsscriptwriter`⁵ (Sebastian et al. 2024). It uses both AIPS and CASA tasks to carry out the initial editing and flagging of bad data. The pipeline uses standard procedures in AIPS to calibrate and image the data. The GMRT image of the galaxy at 610 MHz is shown in Figures 5 (top).

The spectral index image made using the VLA 5 GHz D-array and GMRT 610 MHz images convolved to the same beam size is presented in Figure 4. We find that the average spectral index value in the inner lobes is -1.14 ± 0.09 , while the average spectral index in the outer western lobe is -1.89 ± 0.13 and outer eastern lobe is -1.89 ± 0.17 .

⁵ <https://github.com/binysebastian/aipsscriptwriter>

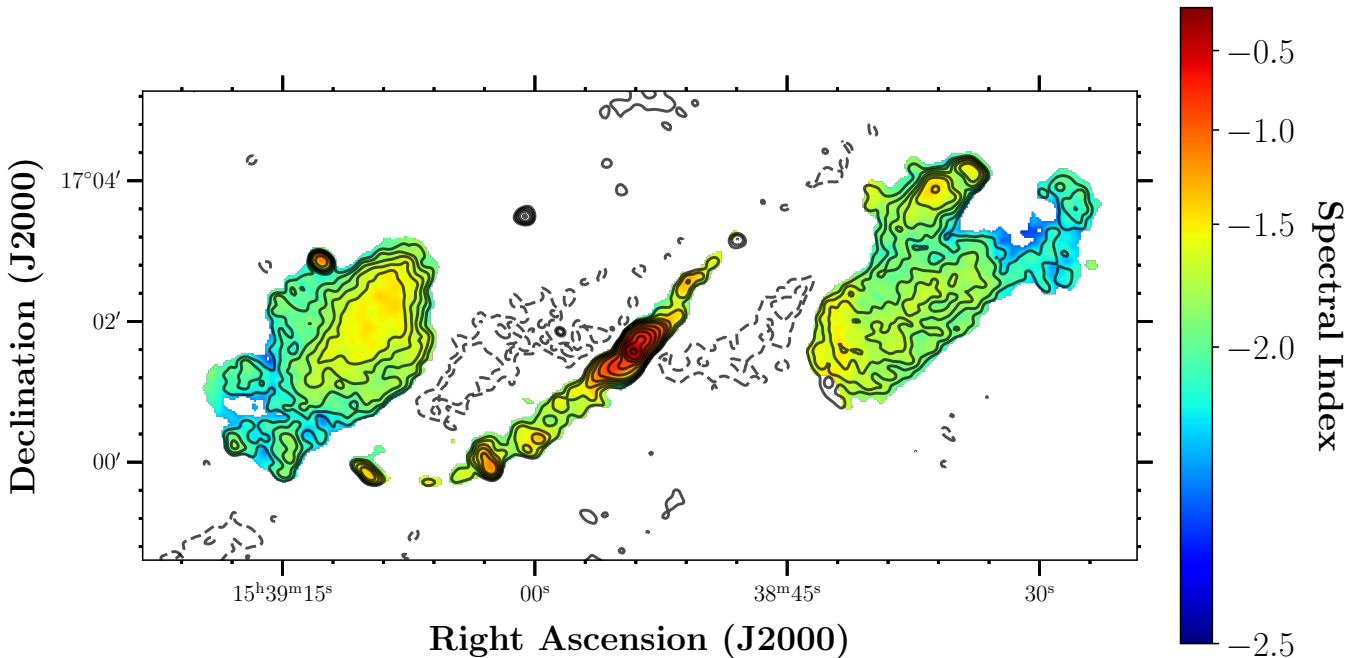


Figure 4. Spectral index image from VLA 5 GHz and GMRT 610 MHz data in color overlaid with 5 GHz total intensity contours. The contours are at $3.5\text{E-}05 \times (\pm 1.4, -1, 1, 1.4, 2, 2.8, 4, 8, 16, 32, 64, 128, 256, 512, 1024, 2048)$ Jy beam $^{-1}$.

4. RESULTS

4.1. Morphologies

NGC 5972 is categorized as a Seyfert type-2 galaxy with a distinctive arrangement of ionized gas, featuring a striking double-lobed structure (Veron & Veron-Cetty 1995). It has an EELR with radius of ~ 12 kpc, which can be seen in images shown in Keel et al. (2015) and Finlez et al. (2022), revealing rich filamentary structures.

Furthermore, NGC 5972 presents compelling findings in the literature that are indicative of past AGN activity (Finlez et al. 2022; Harvey et al. 2022). Finlez et al. (2022) had conducted an ellipse fitting analysis of the F621M HST image, revealing multiple asymmetric tidal structures within a few kpc from the center. The formation of these structures is discussed by Keel et al. (2015); Finlez et al. (2022) as a probable result of past mergers or interactions. Twisted dust structures can also be observed near the central region in the HST image. Keel et al. (2015) conducted an extensive analysis on these intertwined dust lanes, and proposed a differentially precessing, warped disk model (Steiman-Cameron et al. 1992) as the most plausible explanation for these structures. The GMRT 610 MHz image and VLA 5 GHz images display the presence of outer radio lobes, extending up to ~ 250 kpc in radius (Figure 5) which is remarkable, considering that in typical Seyfert galaxies, the radio lobes can usually be traced out to

only a few tens of kpc (Baum et al. 1993; Colbert et al. 1996; Gallimore et al. 2006; Sebastian et al. 2020), making NGC 5972 a rare case to study.

The left panel of Figure 6 presents the VLA 5 GHz B-array uv -tapered total intensity contour image of NGC 5972. The uv -tapering was carried out at 20 k λ for the last self-calibrated visibility data (keeping all the antennas) in order to bring out the diffuse emission better. We detect a radio core and a pair of radio lobes extending in the northwest-southeast direction. The right panel of Figure 6 presents the VLA 5 GHz B-array total intensity contour image overlaid with electric fractional polarization (χ) vectors in red. We find that the northwestern jet/lobe region is highly linearly polarized with a fractional polarization of $15 \pm 3\%$. According to the synchrotron theory, the magnetic fields are inferred to be perpendicular to the χ vectors for optically thin regions like jets and lobes, whereas parallel for optically thick regions like the core. In NGC 5972, the inferred magnetic fields in the jet/lobe region are found to be largely poloidal, i.e. aligned with the jet direction (similar to FR II jets; Bridle et al. 1994). We also note that, using different strategies and different calibrators, the core shows around $1.2 \pm 0.3\%$ polarization which needs to be confirmed with additional data.

Adding further intrigue to this source is the alignment of the emission line structure with its radio counterpart, as illustrated in Figure 7.

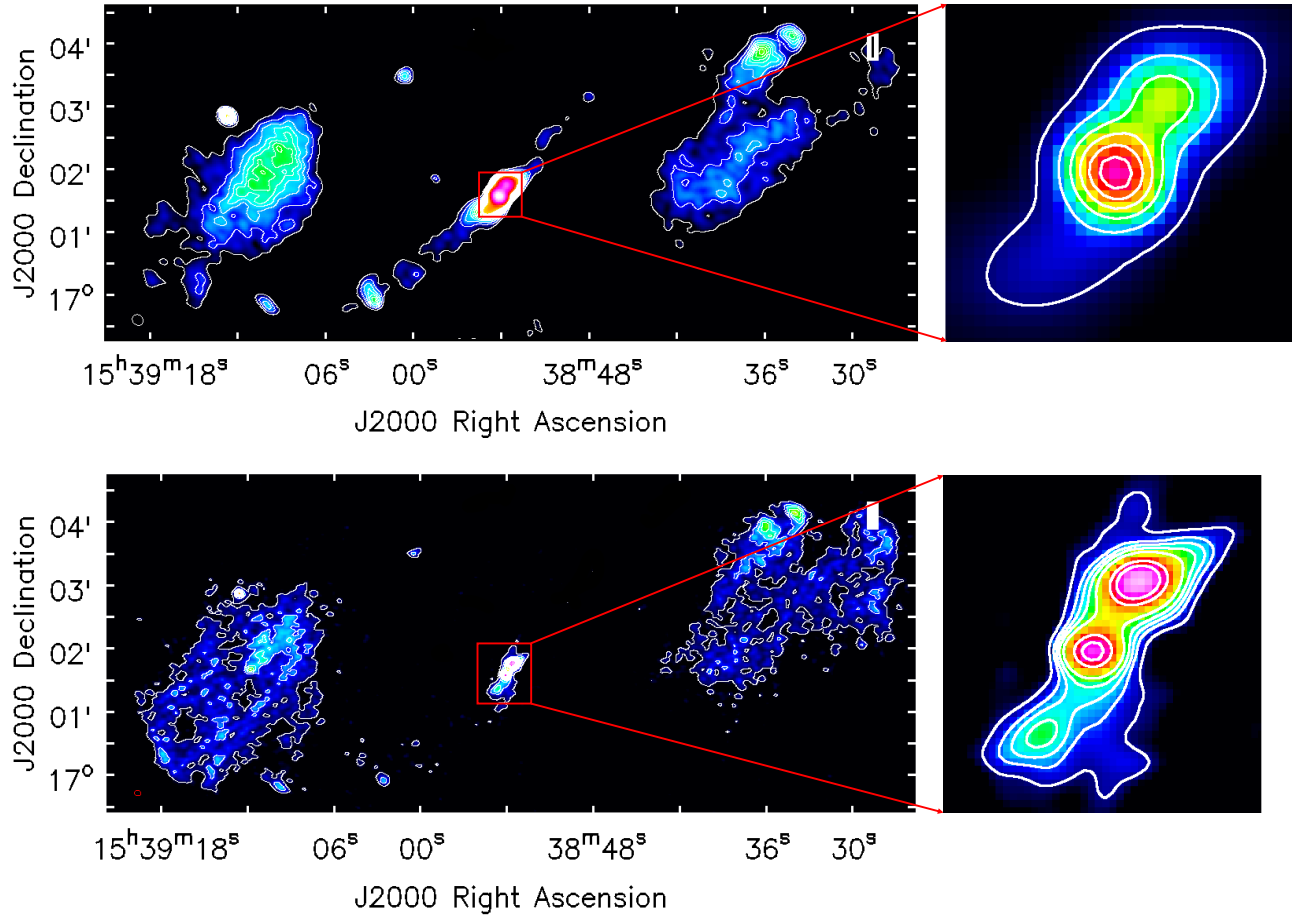


Figure 5. Top: Archival VLA D-array image at 6.0 GHz. Bottom: GMRT image at 610 MHz. The contour levels used are: $3\sigma \times (1, 2, 4, 8, 16, 32, 64)$, where $\sigma = 45.5 \mu\text{Jy beam}^{-1}$ for 6 GHz VLA image, and $\sigma = 98.2 \mu\text{Jy beam}^{-1}$ for GMRT 610 MHz image.

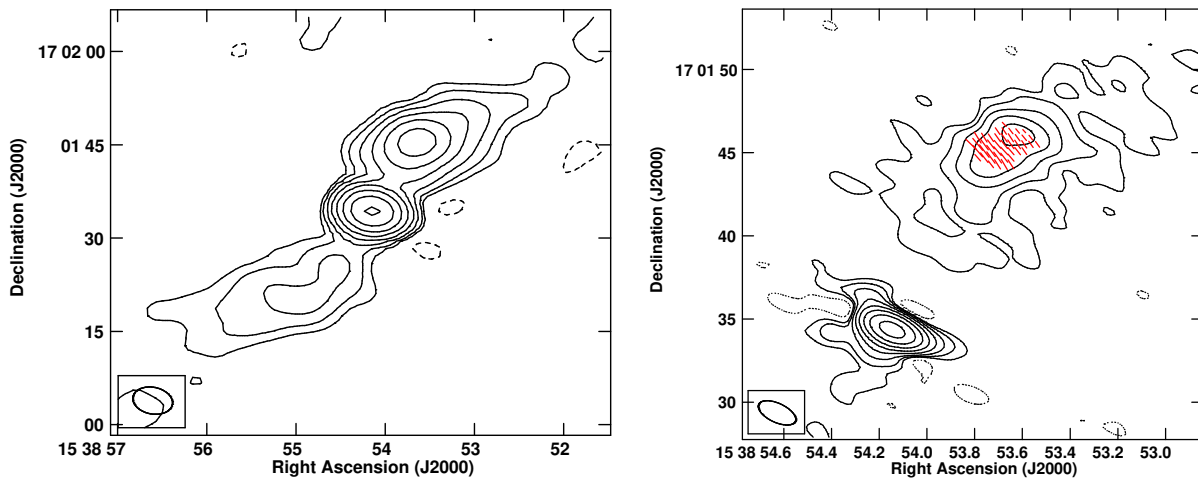


Figure 6. Left: VLA 5 GHz B-array uv -tapered total intensity contour image superimposed with electric fractional polarization vectors in red. $1''$ length of the vector corresponds to 25% fractional polarization. The peak contour flux density is $x \text{ mJy beam}^{-1}$ and the contour levels are $y \times (-1, 1, 2, 4, 8, 16, 32, 64, 128, 256, 512) \text{ mJy beam}^{-1}$, where $(x, y) = (5.0; 0.0350)$ for the left panel and $(4.9; 0.0275)$ for the right panel.

4.2. Kinematics

The multi-wavelength IFU data of NGC 5972 provide valuable insights into various aspects of the galaxy’s dynamics, including the outflow patterns, gas distribution, and the correlation between the AGN jet and the surrounding gas. Results obtained after the Gaussian fitting (refer to section 3.1) were used to estimate the gas kinematics. Panels in Figure 1 show the stellar velocity and stellar dispersion maps and Figure 7 shows [O III] and H α flux maps, gas velocity and residual velocity for both narrow and broad Gaussian components. The residual maps are created by subtracting the emission line gas velocity and the stellar velocity.

The EELR exhibits a distinct velocity profile aligned with the radio jet in the north-south direction, effectively tracing the path of the jet. From the velocity maps it is evident that the gas demonstrates rotational behavior, as indicated by the observed blueshift in the lower structure and redshift in the upper structure. For the [O III] emission line, the narrow component exhibits average gas velocities of 163 ± 68 km s $^{-1}$ in the north and -208 ± 71 km s $^{-1}$ in the south. In contrast, the broad component shows average velocities of 132 ± 51 km s $^{-1}$ and -182 ± 28 km s $^{-1}$ for the north and south regions, respectively. For the H α emission line, the narrow component has average gas velocities of 192 ± 34 km s $^{-1}$ in the north and -162 ± 42 km s $^{-1}$ in the south, while the broad component reveals average velocities of 115 ± 47 km s $^{-1}$ and -129 ± 23 km s $^{-1}$ in the north and south regions, respectively. Detailed discussion about the implication of the residual velocity maps are presented in section 5.2.2.

4.3. Electron density estimates

Electron density is one of the important parameters in determining the energy estimates from the AGN. Both mass outflow rates and kinetic luminosity depend significantly on the electron density of the outflow. The optical emission lines such as [S II] $\lambda 6716, 6731$ (referred to as the [S II] doublet) or [O II] $\lambda 3726, 3729$, provide direct measurements of this density (Osterbrock & Ferland 2006; Sanders et al. 2016; Kaasinen et al. 2017; Harrison et al. 2018; Kakkad et al. 2018; Rose et al. 2018). These emission lines are used because they exhibit relative flux values that solely rely on the electron density occupying specific meta-stable energy levels. For our study, we have used [S II] doublets due to the limited spectral resolution of the MUSE instrument.

Figure 8 (left) shows the electron density map derived using the relation given in Osterbrock & Ferland (2006):

$$n_e = \frac{100\sqrt{T_e}(R - 1.49)}{5.61 - 12.8R} \quad (1)$$

where the flux ratio $R = ([S II]\lambda 6716 / [S II]\lambda 6731)$ and $T_e = 10000$ K is assumed to be initial temperature condition. In the case of the Gaussian 1, the average electron density is ≤ 300 cm $^{-3}$. While for the Gaussian 2 component, which is assumed to mimic the outflowing motion of the gas (as discussed in section 5.2.3), we observe that the electron density is notably higher in the region near the galactic core, around 800 cm $^{-3}$, and gradually decreases as it extends away from the center along the trajectory of the jet, reaching approximately 300 cm $^{-3}$. These values closely align with those reported in the study by Harvey et al. (2022). Radio contours (610 MHz) are overlaid on top to obtain an understanding of the electron density along the path of the jet.

4.4. Resolved BPT diagnostics

Several mechanisms can contribute to the ionization of ISM: photoionization due to star formation or AGN, shock ionization due to stellar winds, jets, or other dynamical processes. To understand the processes at play, optical emission line ratio diagnostics, known as “BPT diagrams” (Baldwin et al. 1981; Veilleux & Osterbrock 1987) are used. We have used [O III]/H β versus [N II]/H α emission line ratios to investigate the ionization mechanism in the galaxy for the individual MUSE bins, which are plotted on the BPT diagram (Figure 9). The dashed line (Kewley et al. 2001) represents theoretical starburst models, while the solid line (Kauffmann et al. 2003) serves as an empirical composite boundary in the [N II]/H α BPT diagram. The region formed in between these boundaries is referred to as, “composite region”, which represents galaxies that exhibit spectral characteristics indicative of both star formation and AGN activity. The dash-dotted line represents the separation between Seyfert-2 and LINERs (Schawinski et al. 2007). We have over-plotted the GMRT contours on top of the reconstructed MUSE image which shows that the jet overlaps with the AGN photo-ionized region, while shock ionization is observed in the perpendicular direction to the jet.

The categorization of LINERs itself is challenging due to ongoing debates about their ionization sources. The uncertainty revolves around whether ionization is primarily driven by an AGN (Ferland & Netzer 1983), fast shocks (Baldwin et al. 1981; Dopita & Sutherland 1995), or due to the ultraviolet radiation emitted by hot old stars (Cid Fernandes et al. 2011; Singh et al. 2013). Therefore, relying solely on the BPT diagram, we cannot determine the specific mechanism responsible for driving feedback in the galaxy. For NGC 5972, Finlez et al. (2022) demonstrated that the stellar population distribution features older populations at the cen-

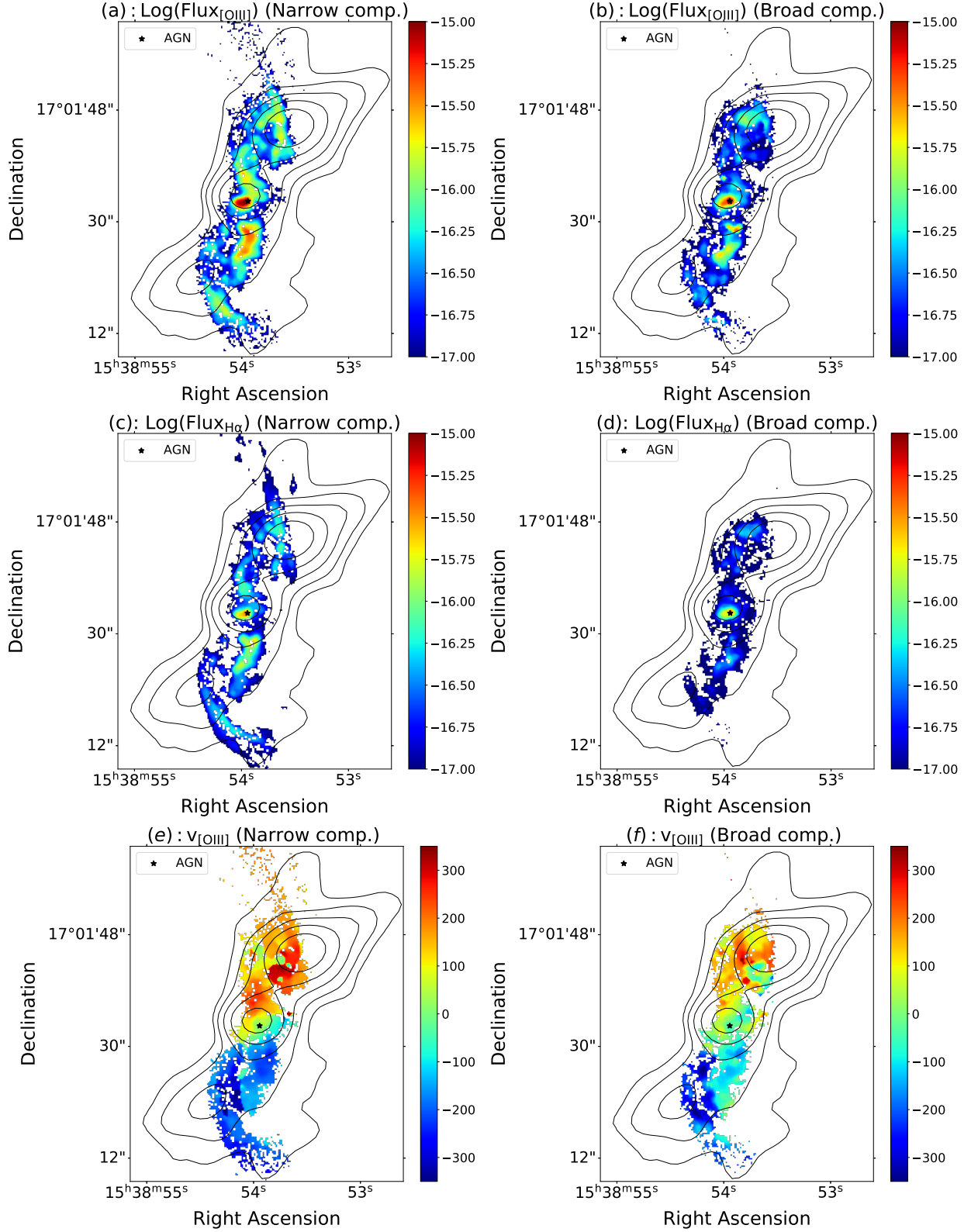


Figure 7. Maps obtained after double Gaussian fitting for [O III] and H α emission lines. (a) - (d): flux maps. (e) - (h): line-of-sight velocity maps. (i) - (l): residual velocity created using the difference between gas velocities and stellar velocity. The flux maps are in $\text{erg s}^{-1}\text{cm}^{-2}$, whereas all the velocity maps are in km s^{-1} . SNR cut of 3σ is applied, where $\sigma = (15, 10) \times 10^{-20} \text{ erg s}^{-1}\text{cm}^{-2}\text{\AA}$ for the [O III] and H α peak flux density respectively. The black contours trace the radio emission from the jet at 610 MHz.

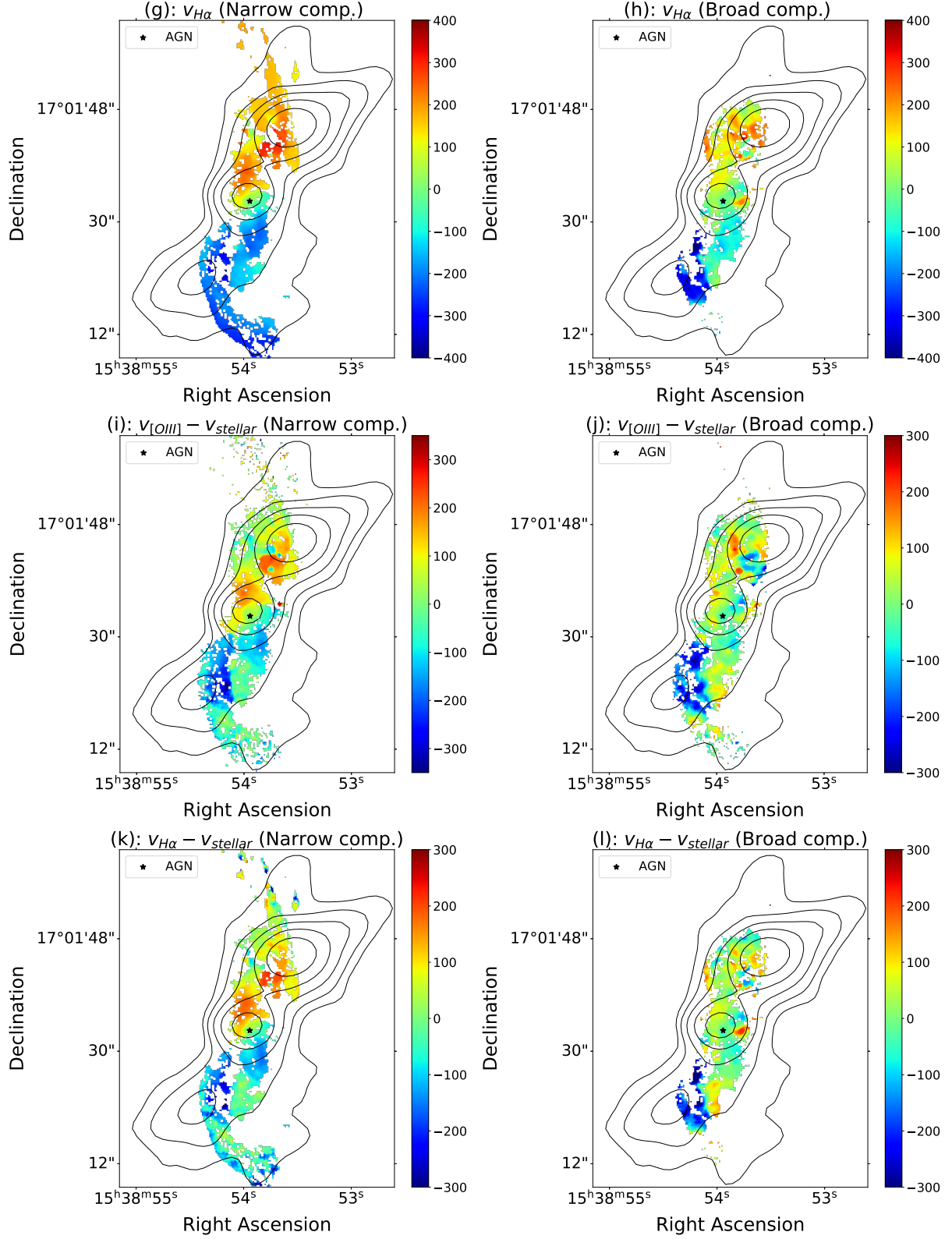


Figure 7. Continued.

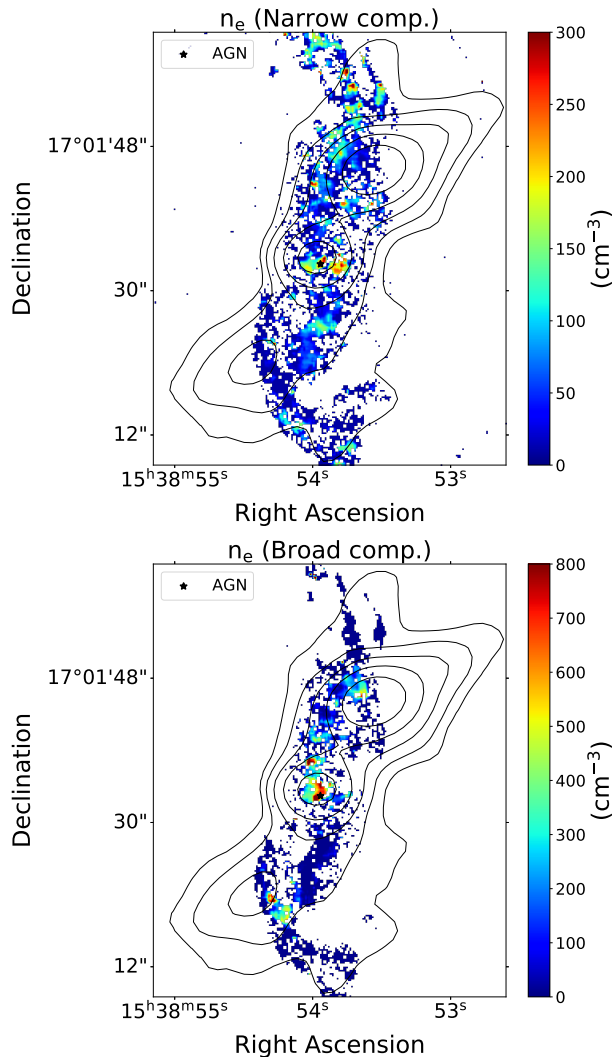


Figure 8. Electron density maps derived from the $[\text{S II}]\lambda 6716/[\text{S II}]\lambda 6731$ line ratio. The top panel represents the electron density for Gaussian 1 and the bottom panel represents the electron density for Gaussian 2. The contour corresponds to 610 MHz radio emission.

ter and younger populations at larger radii, ruling out the contribution of old stars to LINER emission. To validate the most suitable model for explaining the excitation pattern in the LINER, we conducted the shock modeling analysis.

4.5. Shock modeling

We used the radiative shock model database by Alarie & Morisset (2019), calculated with MAPPING V (Sutherland et al. 2018), to obtain the shock models. The models include two scenarios: simple shocks and shocks with precursors. In the simple shocks case, shocks arise from the intense interaction between AGN winds/ jets with the surrounding ISM, leading to colli-

sionally ionized gas. Whereas, in the shock+precursor case, the shock-heated gas produces photons that move upstream, ionizing the gas ahead of the shock front. This model is typically used in situations where both photoionization and shock excitation occur, such as in LINERs (Molina et al. (2018)). Figure 9 shows an overplot of our data on the shock and shock+precursor models for $[\text{O III}]/\text{H}\beta$ vs $[\text{N II}]/\text{H}\alpha$ BPT diagram. Each data point represents a Voronoi bin of the MUSE cube and is color-coded according to its position on the BPT diagram (Figure 9).

To obtain the models, we have chosen the input parameters in the following way: the values for the shock velocities (v_s) were selected based on the result obtained in Section 7. Vacancies were restricted to fall within the range of $v_s = (0 - 350) \text{ km s}^{-1}$. The metallicity was taken as solar as mentioned in Keel et al. (2015) for NGC 5972. The MAPPINGS V models provide a huge range of magnetic field strength, but we have adopted $B = (0.5 - 500) \mu\text{G}$ for all the models since this is a typical range of magnetic fields in Seyfert galaxies (de Bruyn & Wilson 1978b; Bicknell et al. 1998; Kharb et al. 2016; Sebastian et al. 2019a). In general, AGN cover a broad range of radio strengths, and the strength of the resulting magnetic field depends on both the strength and the morphology of the radio emission (Condon & Ransom 2016). The pre-shock electron density was varied between $10 - 1000 \text{ cm}^{-3}$ to check how the model performance varies with different density levels. It has been observed that the shock+precursor model with high-density value; $n_e = 1000 \text{ cm}^{-3}$ (Figure 9, right) is partially consistent for the spaxels that fall in the AGN region in the diagnostic diagram. If large-scale shocks indeed ionize the gas in NGC 5972, then the pure shock models should be able to replicate the LINER fluxes of the emission lines in the BPT diagram. We observe that both low and high-density pure shock models (Figure 9) are able to reproduce the expected LINER emission.

5. DISCUSSION

The radio emission observed in Seyfert galaxies are believed to originate primarily due to three main reasons: (i) jet-related activity (Veilleux 1991; Spoon & Holt 2009; Mullaney et al. 2013; Morganti et al. 2015, 2016; Nesvadba et al. 2017a; Venturi et al. 2023a; Singha et al. 2023), (ii) influence of winds leading to the acceleration of thermal electrons to relativistic energies at shocks (Stocke et al. 1992; Wang 2008; Jiang et al. 2010; Ishibashi & Courvoisier 2011; Faucher-Giguère & Quataert 2012; Zubovas & King 2012; Zakamska & Greene 2014) and/or (iii) star-forming processes (Rosario et al. 2013).

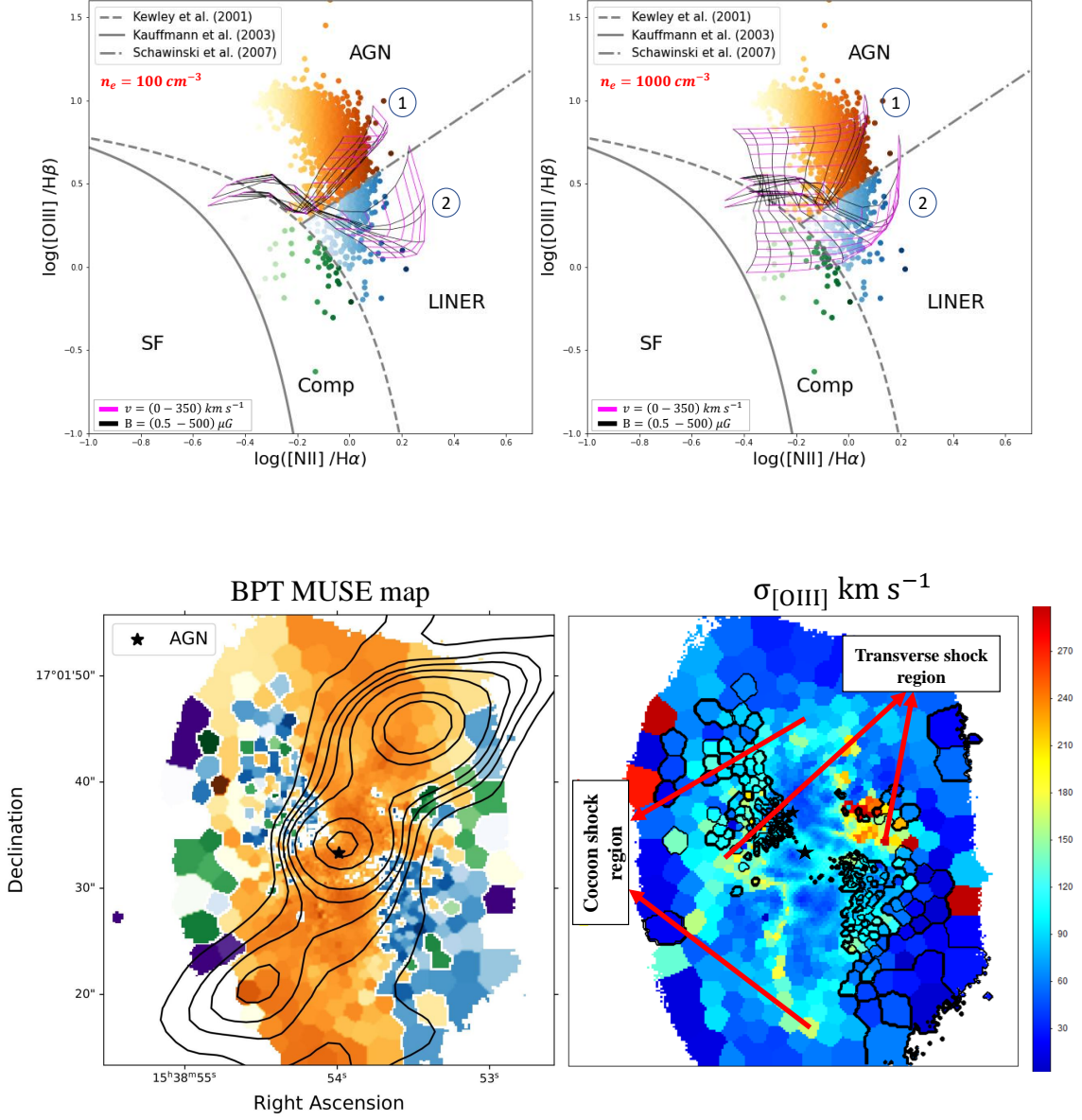


Figure 9. Top: Spatially resolved $[\text{O III}]/\text{H}\beta$ vs $[\text{N II}]/\text{H}\alpha$ diagnostic diagram. The lines in each panel show the theoretical separation between various line excitation mechanisms (refer to Section 4.4). Each point corresponds to a MUSE bin. Shock and shock+precursor models created using MAPPINGS V, are over-plotted on the top. 1: Shock+precursor model, 2: Pure shock model. The magenta grids represent the shock velocities in the range of $v_s = (0-350) \text{ km s}^{-1}$ whereas the black grids represent magnetic field strength within the range $B = (0.5 - 500) \mu\text{G}$. The metallicity is assumed to be solar for both models. For the left Figure, the pre-shock electron density is taken as $n_e = 100 \text{ cm}^{-3}$, while for the right Figure, it is assumed to be $n_e = 1000 \text{ cm}^{-3}$. Bottom left: MUSE cube constructed using the corresponding bins from the BPT diagram. 610 MHz radio contours are overlaid on the top. The data points represent the bins created from the GIST pipeline from the MUSE cube with an SNR of 20. Bottom right: Voronoi binned $[\text{O III}]$ dispersion velocity map. The black regions represent the LINER region from the MUSE BPT map.

The main goal of our work is to study the jet-related feedback that leads to the formation of the remarkable EELR in NGC 5972. We found two main observational signatures of radio-mode feedback: (i) a spatial connection of the radio jet with shocked regions, and (ii) the presence of gas outflows coincident with the radio jets or evidence for acceleration/deceleration of the gas by the jets.

5.1. Energetics of different components

5.1.1. Jet kinetic power

There are several studies, such as [Bîrzan et al. \(2004, 2008\)](#); [Merloni & Heinz \(2007\)](#); [Cavagnolo et al. \(2010\)](#) that give an empirical relation between jet power and radio luminosity. These studies mostly utilize lower frequency data ($\nu \leq 1.4$ GHz) to obtain the flux density of the radio feature. [Merloni & Heinz \(2007\)](#) have derived the jet power and radio luminosity relation using 5 GHz radio data for a sample of low- luminosity radio galaxies. Since we already acquired the 5.5 GHz VLA data, we have used the equation given by [Merloni & Heinz \(2007\)](#) to calculate the jet power in the nuclear region:

$$\log(P_{\text{jet}}) = (0.81 \pm 0.11) \log(L_{5 \text{ GHz}}) + 11.9_{-4.4}^{+4.1} \quad (2)$$

From the VLA 5.5 GHz data, we have estimated the core flux density to be 5.2 mJy (spectral index $\alpha = -0.7$) which corresponds to $\sim 10^{38}$ ergs s^{-1} core luminosity. Hence using the above relation, we obtained $\log(P_{\text{jet}}) = 43.23_{-8.66}^{+8.36}$ ergs s^{-1} .

5.1.2. AGN kinetic power

We assume that a fraction (5%) of the AGN bolometric luminosity (L_{bol}) is converted into AGN kinetic power that drives the jet through the interstellar medium ([Di Matteo et al. 2005](#); [Nesvadba et al. 2017b](#)). For NGC 5972, $L_{\text{bol}} \approx 10^{44}$ ergs s^{-1} ([Keel et al. 2017](#)), therefore $\dot{E}_{\text{AGN}} \approx 10^{42}$ ergs s^{-1} .

5.1.3. SFR mechanical power output

We have estimated the star formation rate (SFR) using IRAS 60 μm and 100 μm fluxes. Note that the SFR derived from these fluxes includes contributions from the AGN at FIR, as it has not been corrected for AGN influence. We have taken this into account for our subsequent calculations. The relation used to derive the SFR is given by [Kennicutt \(1998\)](#):

$$\text{SFR} (M_{\odot} \text{ yr}^{-1}) = 4.5 \times 10^{-44} L_{\text{FIR}} \quad (3)$$

where $L_{\text{FIR}} = 4\pi D^2 \times \text{FIR} \times L_{\odot}$, and $\text{FIR} = 1.26(2.58f_{60} + f_{100}) \times 10^{-14}$ ([Helou et al. 1988](#)). The SFR comes out to be $4.17 M_{\odot} \text{ yr}^{-1}$. We have also estimated the SFR from the 1.4 GHz NVSS data using the

relation given in [Condon \(1992\)](#) (equation 21), which comes out to be $73 M_{\odot} \text{ yr}^{-1}$. The difference in SFR estimated from IR and radio data suggests that the excess radio emission likely stems from sources other than star formation, such as radio jet or winds. Given that the galaxy is ‘‘radio-loud’’ with radio emission extending to 550 kpc as observed in [Figure 5](#), it is unlikely that this excess radio emission is driven by the winds.

To estimate the net mechanical power output from star formation, we followed the method by [Schaye & Dalla Vecchia \(2008\)](#), which suggests that if the kinetic energy injected per solar mass of stars formed is $\epsilon_{\text{SN}} \approx 1.8 \times 10^{49}$ ergs M_{\odot}^{-1} , then about 40% of this energy is carried away by the winds, while the rest is radiated away. Thus, the net mechanical injection rate into the galaxy from star formation (\dot{E}_{SFR}) is $0.72 \times 10^{49} \times \text{SFR}$ ergs s^{-1} . For NGC 5972, \dot{E}_{SFR} derived from IR data is 9.5×10^{41} ergs s^{-1} .

5.1.4. Can the jet inflate the EELR?

To quantify whether the jet is capable of pushing the gas at 10s of kpc distance, we have estimated the PV amount of work done on the gas by the jet. A spherical approximation for the EELR volume is used to simplify and provides a practical estimate of the volume. Pressure on the gas is calculated as $P = nK_{\text{B}}T$, where K_{B} is the Boltzmann constant.

To calculate the PV amount of work done on the EELR, we considered two phases of the ISM. For the cooling phase or post-shock gas, we assumed a temperature of 10^4 K and a density $\leq 1000 \text{ cm}^{-3}$. For the gas around the AGN, where the shocked gas is assumed to be hotter, we used temperature estimates from [Harvey et al. \(2022\)](#) APEC modeling, corresponding to a temperature range of ($10^6 - 10^7$ K), with an assumed density $\leq 100 \text{ cm}^{-3}$. The PV work done comes out to be approximately between 10^{51-55} ergs. Assuming $P_{\text{jet}} \approx 10^{43}$ ergs s^{-1} (section 5.1.1) and the spectral age of the inner radio jet to be 20 Myr (refer to section 5.3), we have estimated the time-averaged power of the jet, which comes out to be 1.08×10^{58} ergs. Thus, comparing the jet power and the PV work done on EELR, indicates that only a small fraction (0.00027 - 0.27)% of the jet’s total power is enough to do the work on EELR.

5.2. Jet-medium interaction

In the following sections we discuss the evidences of jet-ism interaction and how jet influences the medium.

5.2.1. Transverse shock and enhanced velocity dispersion

When the relativistic jet interacts with the surrounding gas, rapid shocks can induce ionization in the gas medium. This ionized gas emits distinctive spectra and

can provide insights into the physical characteristics of the shocks. Typically, line ratios within the narrow-line region suggesting the presence of shocks are positioned within the LINER region of optical BPT diagrams (Mingozzi et al. 2019; Perna et al. 2020; Cazzoli et al. 2022). In our study, we have detected LINER excitation in the region perpendicular to the jet (section 4.5). The emergence of these transverse LINER regions, as illustrated in the resolved BPT diagram (see Figure 9, bottom left), may signify the existence of a jet-induced shock propagating perpendicularly to the jet axis. Consistence with the literature (Couto et al. 2013; Lena et al. 2015; Couto et al. 2017; Finlez et al. 2018; Ruschel-Dutra et al. 2021; Venturi et al. 2021), we have also observed enhanced [O III] line width in the direction perpendicular to the radio jet (Figure 9, bottom right). While our observations do not show a drastic enhancement ($v \geq 250 \text{ km s}^{-1}$) as reported in these studies, we do observe shocked region with an inflated-shell-like structure, exhibiting higher velocity dispersion compared to the inner region. We calculated the average [O III] dispersion for both the shocked region and the inner region, which comes out to be $158 \pm 55 \text{ km s}^{-1}$ and $63 \pm 13 \text{ km s}^{-1}$ respectively.

The observed shock structure raises questions about its geometry, potentially indicating either a planar or cocoon shock (Wagner & Bicknell 2011; Wagner et al. 2012; Mahony et al. 2016). A planar shock suggests a flat, extended shock front, uniformly compressing and heating gas perpendicular to the jet axis, likely from direct jet-medium interaction. Conversely, in a cocoon shock structure, the jet propagates through the surrounding medium, compressing and heating it as it moves. As the jet advances, it creates a cavity ‘‘cocoon’’ of shocked gas surrounding it. The observed structure in the [O III] dispersion velocity map (Figure 9, right) could be indicative of a cocoon shock.

5.2.2. Outflows: Enhanced velocities along the jet

The gas dynamics within the EELR can be shaped by multiple contributing factors. Firstly, the gravitational potential of the host galaxy plays a pivotal role, it not only dictates the motion of stars but also exerts its influence on the gas in the EELR (Schiano 1986; Nelson & Whittle 1996). Furthermore, the presence of radiation (Fabian 1999; Murray et al. 2005; Thompson et al. 2015), or thermal pressures (Davidson & Netzer 1979; Krolik & Vrtilik 1984; Dannen et al. 2020; Kumar & Mukhopadhyay 2021), stemming from the central AGN/starburst or even the AGN jets (Tadhunter et al. 1989; Emonts et al. 2005; Holt et al. 2008; Ishibashi et al. 2013; Mahony et al. 2016; Villar-Martín et al. 2017; Jarvis et al. 2019) can trigger the ejection of gas, result-

ing in outflows. To distinguish between these contributions, we study the residual maps, which is the difference between emission line gas velocity and stellar velocity. Figure 7 (i) - (l), shows the residual velocity maps created for the [O III] and $\text{H}\alpha$ emission lines for both Gaussian components. While several studies typically use the broad component to characterize outflows, e.g., (Harrison et al. 2014; Singha et al. 2022), our broad and narrow component residual maps reveal that the broad component closely follows the stellar velocity, whereas the narrow component exhibits a significant offset. This suggests that the narrow component has additional velocity beyond what is expected from the galaxy’s gravitational effects. This offset could be due to the outflowing gas, which may be experiencing a systematic velocity shift as it is pushed away by the jet. Hence, we referred the narrow Gaussian component as the outflowing component for the galaxy.

Harvey et al. (2022) reports the presence of a nuclear outflow (referred as ‘‘[O III] bubble’’) in the north-east direction, within a proximity of $2''$ (1.2 kpc) from the center. They found the outflow velocities reaching up to 300 km s^{-1} . The average gas velocity calculated from our narrow component [O III] and $\text{H}\alpha$ residual maps, comes out to be $212 \pm 33 \text{ km s}^{-1}$ and $130 \pm 18 \text{ km s}^{-1}$ respectively. Since, we are measuring line-of-sight velocities, we suspect that the actual outflow velocities might be substantially higher, depending on the inclination of the EELR.

5.2.3. Outflow energetics

To understand the outflow characteristics, we study the mass outflow rate of the galaxy. We focused on the physical parameters associated with the narrow Gaussian component to determine the outflow properties. Initially, we calculated the gas mass within the outflow using [O III] and $\text{H}\alpha$ emission lines, employing the equations outlined in Venturi et al. (2023b), which rely on the relationship previously established by Carniani et al. (2015) and Fiore et al. (2017):

$$\frac{M_{\text{out},\text{H}\alpha}}{M_{\odot}} = 0.6 \times 10^9 C \left(\frac{L_{\text{H}\alpha}}{10^{44} \text{ erg s}^{-1}} \right) \left(\frac{n_e}{500 \text{ cm}^{-3}} \right)^{-1} \quad (4)$$

$$\frac{M_{\text{out},[\text{O III}]}}{M_{\odot}} = 0.8 \times 10^8 \left(\frac{C}{10^x} \right) \left(\frac{L_{[\text{O III}]}}{10^{44} \text{ erg s}^{-1}} \right) \left(\frac{n_e}{500 \text{ cm}^{-3}} \right)^{-1} \quad (5)$$

Wherein, we set $C = \langle n_e \rangle^2 / \langle n_e^2 \rangle$ to unity. $x = [\text{O}/\text{H}] - [\text{O}/\text{H}]_{\odot}$, where we consider [O/H] to be solar oxygen abundance. We assume the gas temperature $T \simeq 10^4 \text{ K}$, and electron density n_e is calculated using equation 1.

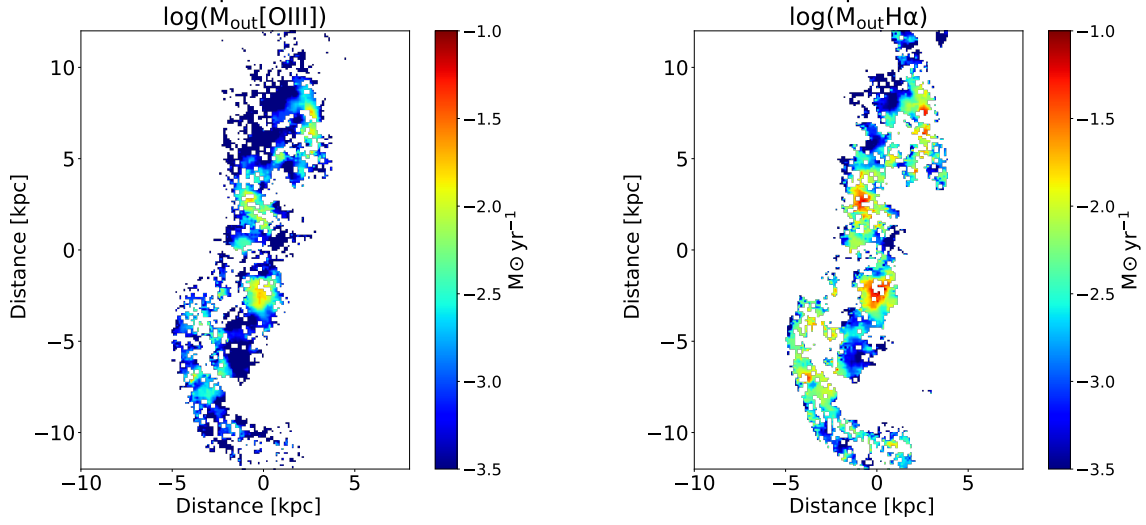


Figure 10. Plots showing trends of mass outflow rate with distance. The positive value of distance corresponds red-shifted region, while the negative distance corresponds to the blue-shifted region of the galaxy.

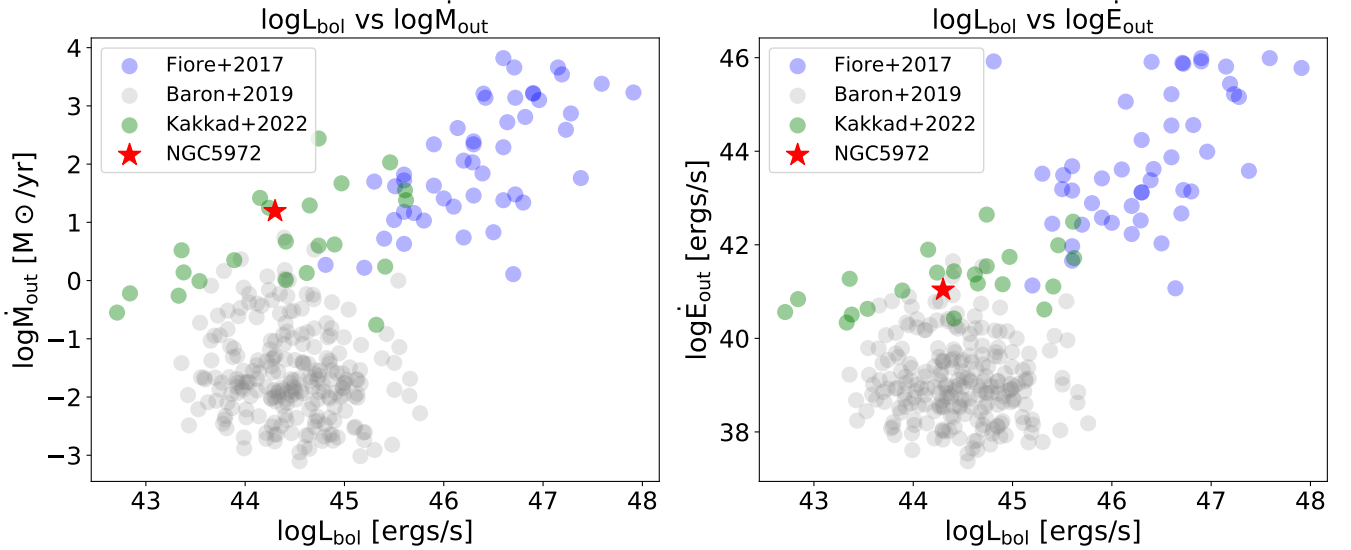


Figure 11. Left: Mass outflow rate as a function of AGN bolometric luminosity. Right: outflow kinetic power as a function of AGN bolometric luminosity. The blue data points represent the ionized outflow measurements reported by [Fiore et al. \(2017\)](#). The green data points represent the ionized outflow measurements reported by [Kakkad et al. \(2022\)](#). The grey data points represent samples from [Baron & Netzer \(2019\)](#), while the red star is our target, NGC 5972.

Assuming that the density $\rho(r)$ and the outflow velocity $v(r)$ are constant within a spaxel of thickness ΔR , the average outflow rate across each spaxel can be calculated. This leads to a simplified expression for the radial average mass outflow rate as:

$$\dot{M}_{\text{out}} = \frac{M_{\text{out}} v_{\text{out}}}{\Delta R} \quad (6)$$

Where M_{out} is the mass of the outflow gas calculated using equations 4 and 5, ΔR is the width of the spaxel (~ 0.1 kpc), and v_{out} is the outflow velocity, $v_{\text{out}} \approx v_{\text{res}}$, where $v_{\text{res}} = v_{[\text{O III}]} - v_{\text{stellar}}$ is the residual velocity of the

narrow component used as a proxy for the outflow velocity. From Figure 10, it is observed that both outflows are concentrated near the center. However, [O III] outflows are more tightly confined within approximately 5 kpc radius, whereas, H α emissions extend out upto ~ 10 kpc radius.

We have also computed the kinetic power of the outflow as:

$$\dot{E}_{\text{out}} = \frac{\dot{M}_{\text{out}} v_{\text{out}}^2}{2} \quad (7)$$

We found that the value of \dot{E}_{out} using $\text{H}\alpha$ emission line is $4.9 \times 10^{41} \text{ ergs s}^{-1}$, whereas \dot{E}_{out} using $[\text{O III}]$ emission line is $1.09 \times 10^{41} \text{ ergs s}^{-1}$. Comparing the outflow kinetic power with the radio jet power $P_{\text{jet}} \approx 10^{43} \text{ ergs s}^{-1}$, suggests that the jet have a substantial amount of energy available to drive or influence the outflows.

We have compared our results with the literature like [Fiore et al. \(2017\)](#), [Baron & Netzer \(2019\)](#) and [Kakkad et al. \(2022\)](#). All these studies shows a dependence of outflow properties on the AGN bolometric luminosity, with a sample coverage of $L_{\text{bol}} \sim 10^{42} - 10^{48} \text{ ergs s}^{-1}$. For NGC 5972, we adopted the AGN bolometric luminosity value calculated by [Finlez et al. \(2022\)](#), i.e., $2 \times 10^{44} \text{ ergs s}^{-1}$ based on the Gemini IFU observations. In Figure 11, the left panel shows the mass outflow rate and the right panel shows the kinetic power as a function of AGN bolometric luminosity. The red star represents NGC 5972, where the outflow properties were calculated from $[\text{O III}]$ gas. The blue dots represent samples from [Fiore et al. \(2017\)](#), which include AGN ionized winds traced by high-velocity $[\text{O III}]$, $\text{H}\alpha$, and/or $\text{H}\beta$. The green dots represent samples from [Kakkad et al. \(2022\)](#), which feature sub-kiloparsec scale $[\text{O III}]$ ionized gas in low-redshift ($z \leq 0.1$) X-ray AGN. The grey dots represent samples of warm ionised outflows of low-to-moderate luminosity type-II AGN within $z \leq 0.15$, studied by [Baron & Netzer \(2019\)](#). Based on the plots, we observe that NGC 5972 shows trends similar to the [Kakkad et al. \(2022\)](#) samples with outflow mechanisms at a lower luminosity AGN and outflow strength.

5.2.4. Clues from inclination

Although there is a remarkable alignment between the inner jet and the EELR in projection, they need not be spatially coincident in the sky. We try to constrain the inclination angle of the jet in comparison with the EELR in the sky. The disk rotation of NGC 5972 (Figure 1) suggests that the southern part of the galaxy is aligned towards us. Using rotation curve fitting, [Finlez et al. \(2022\)](#) estimated an inclination angle in the range $40^\circ - 50^\circ$ for the stellar emission. The $[\text{O III}]$ emission line gas has a similar orientation as the galaxy (Figure 7) although the mean inclination angle determined by [Finlez et al. \(2022\)](#) is around 15° . They also report that the $[\text{O III}]$ emission profile is complex and not fit with a purely rotational model.

The radio image of the jet can provide additional insight into the orientation of the jet. Based on the surface brightness contrast between the north-western and south-eastern lobes (Figure 5), we expect that the northern jet/lobe is the approaching one if we assume the jet is relativistic. However, it should be noted that such

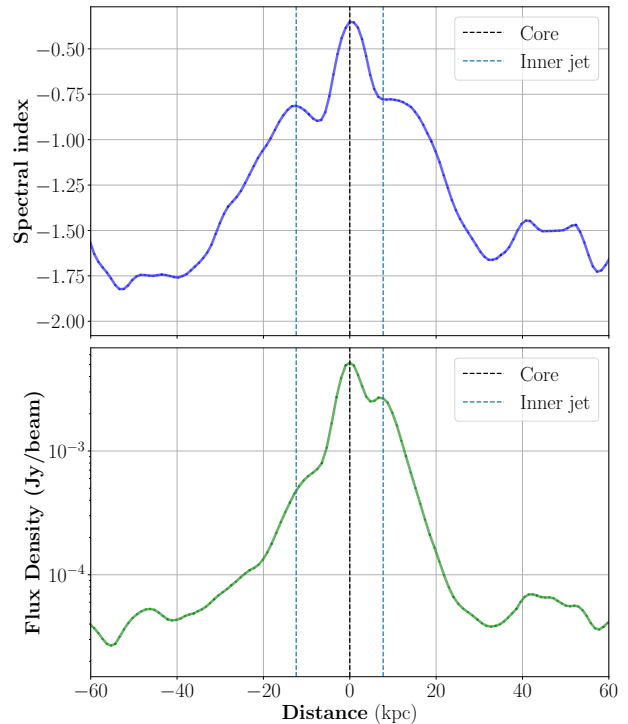


Figure 12. Spatial variation of flux density and spectral index from the core.

asymmetries can also stem from differences in environments. Indeed, the gas in the northern region appears to be denser than in the southern region. For the broad component, the mean electron density in the north is $140 \pm 25 \text{ cm}^{-3}$ compared to $71 \pm 16 \text{ cm}^{-3}$ in the south, and for the narrow component, it is $252 \pm 20 \text{ cm}^{-3}$ in the north and $198 \pm 38 \text{ cm}^{-3}$ in the south.

Another clue comes from the Laing-Garrington effect ([Laing 1988](#); [Garrington et al. 1988](#)), which hypothesizes that the lobe showing higher fractional polarization is pointed towards us due to lesser intervening medium causing lower depolarization. While we detect polarization in the northern lobe with high fractional polarization ($\sim 15\%$), the upper limit on the fractional polarization in the southern lobe is 30% based on a 3σ limit. Hence this method is also inconclusive in the absence of deeper data. Therefore, at this point, we are not able to confirm or reject the spatial coincidence of the jet and EELR in the sky.

5.3. Evidence for episodic activity

The radio images also show evidence of episodic activity. The surface brightness and the spectral index profile show a clear discontinuity along the jet (see Figure 12). The flattening of the spectral index at the location of the surface brightness peak on either side of the core is typical of hotspots. The steeper spectral index just

beyond the apparent inner hotspot suggests that the inner jet is being straddled by the outer jet which consists of relativistic plasma that underwent acceleration much before the inner pair. These features are typical for double-double radio galaxies. It has to be noted, however, that the magnetic field orientation is not typical for hotspot regions. Usually, it is aligned along the edge of the hotspot (due to compression and magnetic field amplification at the edge), whereas in this source the magnetic fields are primarily aligned along the direction of the jet (see Figure 6). Such an alignment might be because the inner jet does not face much obstruction on its path as the outer jet has cleared most of the material out in the previous episode. The inner jets aligning with the outer jets is indeed commonplace in powerful double-double radio galaxies (Sebastian et al. 2018; Marecki et al. 2023), although this is not the case in weaker jet systems (Kharb et al. 2006; Sebastian et al. 2019b; Rao et al. 2023). Another interesting observation is that the core is bright with a relatively flat spectrum (~ -0.35) pointing to a currently active radio core.

The leading explanation for the origin of “Voorwerp” galaxies is that these are Seyfert galaxies showcasing episodic activity. The ‘on’ and ‘off’ timescales in NGC 5972 were studied in detail by Finlez et al. (2022). They studied the radial dependence of the ionization state and estimated a clear increase in L_{bol} with radius. Hence, they argue that the Quasar faded gradually by a factor of 100 over 10000 years.

We estimated the dynamical and spectral ages for the inner and the outer lobes to compare with those estimated by Finlez et al. (2022). We used the equations (1) – (5) from O’Dea & Owen (1987) and Pérez-Torres & Alberdi (2007) to estimate the equipartition magnetic field parameters and the spectral age, respectively. The spectral age calculation is fraught with several uncertainties. Parameters, such as the filling factor and the ratio of proton to electron number densities, both of which were assumed to be unity, remain uncertain and also affect the equipartition magnetic field values, which can, in turn, affect the spectral ages. More importantly, the spectral ages will critically depend on the break frequency. We lack the multi-frequency coverage at similar resolutions to constrain the break frequency accurately. We obtain spectral ages of approximately 20 Myr and 40 Myr by assuming break frequencies of 5.5 GHz and 1.5 GHz, respectively, for both the inner and the outer lobes. The inner lobes likely have a much higher break frequency compared to the outer ones, suggesting the outer lobes have undergone more radiative losses over time, consistent with their older age (e.g., Nandi et al. 2019; Marecki et al. 2016, 2021).

In the absence of the relevant data, we opt to estimate the dynamical ages using a more simplistic approach. Typical FR II hotspots have a mildly relativistic advance speed of 0.1 c to 0.5 c (O’Dea et al. 2009), which remains constant over the lifetime. This advance speed translates to an age range of 1.6-8 Myr and 35-170 Myr for the outer and the inner hotspots, respectively. Note that these ages are lower limits and can be higher depending on the inclination of the lobes in the sky. Furthermore, the current activity of the radio core and the age of the inner hotspots being tens of Myr makes it challenging to align with a scenario where the quasar gradually faded over 10,000 years.

Figure 5 shows that the inner radio jets are not aligned with the outer lobes, indicating a shift in the ejection axis of the radio jet. This shift could be the result of a merger between two galaxies and their central black holes, as suggested by Merritt & Ekers (2002) for X-shaped or Rubinur et al. (2017) for S-shaped radio sources. A plausible scenario is that the jets were initially oriented east-west, powering the lobes. Following the merger, the jet axis shifted. This scenario aligns with the merger evidence discussed in section 4.1. It also implies that the radio lobes are currently aging without a fresh supply of relativistic particles. Furthermore, based on the clear contrast in radio spectral index between the inner and the outer lobe (Figure 4), we propose that the inner radio jet originates from a more recent episode of AGN activity compared to the larger structure, which resembles an FRII narrow-line radio galaxy. The inner structure, with its S-shaped jet, resembles the lobes of a Seyfert galaxy, such as NGC 3516 (e.g., Baum et al. 1993).

5.4. *UV and X-ray emission associated with the EELR: evidence for shock ionization?*

Archival GALEX data of both FUV and NUV emission is available for NGC 5972 (Figure 13). The UV images reveal an extended structure aligned with the radio jet. Although photoionization from the central AGN is a common source of UV emission, it does not fully explain the observed features in NGC 5972. Specifically, the UV emission is neither isotropic nor bipolar and does not decrease monotonously with radius as expected from a purely photoionized model. An alternative explanation for the UV emission could be star forming activities induced by the jet (Gaibler et al. 2012; Duggal et al. 2021, 2023). However, this scenario does not explain the X-ray emission coincident with the jet observed by Harvey et al. (2022).

Chandra observations of NGC 5972 reveal extended soft X-ray emission coincident with the [O III] emission,

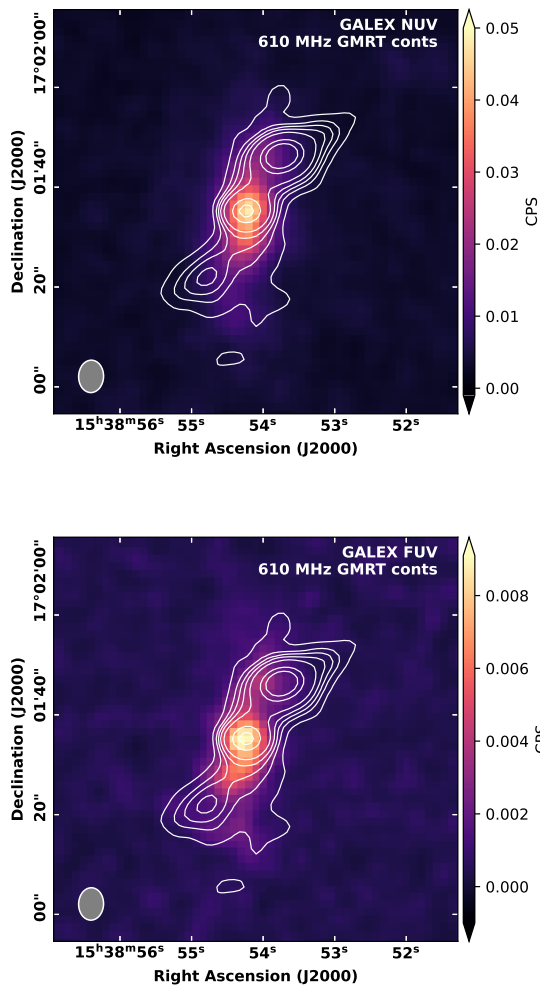


Figure 13. GALEX FUV and NUV band image of NGC 5972 with 610 MHz contours overlaid on the top.

which may be attributed to either shock from a jet (Sutherland & Bicknell 2007; Lanz et al. 2015), a hot wind (Nims et al. 2015), or from AGN photoionized line emissions (Sambruna et al. 2001). Harvey et al. (2022) noted some alignment of X-ray regions with the radio emissions inferred from 3 GHz VLASS data, hinting at a possible connection between the radio jet and X-ray emission. They also observed that the X-ray emission in the southern EELR follows the curved [O III] tail, with the X-ray peak located at a larger distance, suggesting weak shock-induced X-ray emission. Since our 610 MHz radio data provides a better image of the extended radio jet and reveals the southern jet, which shows alignment with UV and optical [O III] emissions, it suggests that the observed X-ray emission could also be attributed to jet-induced shocks. Additionally, APEC modeling by Harvey et al. (2022) indicates EELR temperatures in

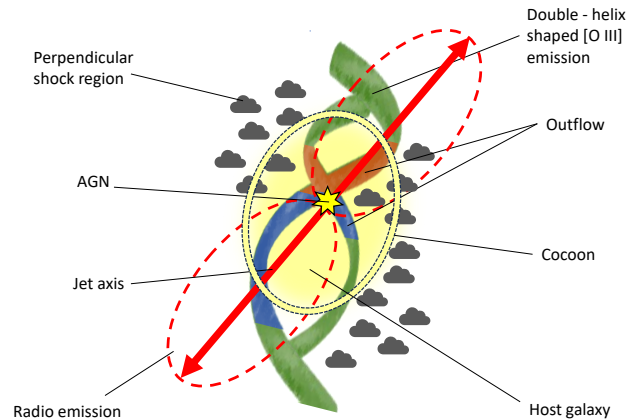


Figure 14. Cartoon schematic diagram showing various mechanisms at play in NGC 5972. The green helix represents the [O III] emission as observed from the HST image. The jet axis is indicated by the red line, and the radio emission is depicted by the dotted red lobes. The black clouds denote the shock regions perpendicular to the jet, as determined by BPT analysis. The red and blue structures represent the outflow region in the galaxy. The shocked cocoon is shown in yellow.

the range from 0.6 to 3.4 keV ($\approx 10^6 - 10^7$ K), which further indicates that such high-temperature gas could be a result of shock heating.

Overall, the shock model provides a simpler and more cohesive explanation for the observed X-ray and UV emission and is consistent with the optical emission line ratios discussed in section 4.4. While the fading quasar model cannot be entirely ruled out, we propose a combined shock+precursor model as the most plausible explanation for ionizing the EELR in NGC 5972. This model accounts for all the multi-wavelength observations and warrants further investigation.

6. CONCLUSIONS

We present a detailed study of NGC 5972, a noteworthy active galaxy having kpc-scale EELR, using VLA L-band and C-band, GMRT 610 MHz radio observations, and IFS VLT/MUSE archival data. Despite previous research suggesting that the EELR is merely a consequence of AGN photoionization, our observations show that the radio jet also plays a significant role. A comprehensive overview of our results is listed below.

1. The morphology of NGC 5972 suggests a dynamic history of the galaxy. A twisted dust lane and a helical-shaped EELR can be explained as a result of a past merger activity or by a precessing disk model as discussed in Keel et al. (2015). Additionally, NGC 5972 showcases an impressive S-shaped

radio structure spanning about 250 kpc in radius (Figure 5), surpassing the typical extents seen in Seyfert galaxies, where radio lobes generally cover only tens of kpc, suggesting a prolonged AGN activity.

2. The velocity maps of [OIII] and H α emission lines provides an intriguing insights of the gas kinematics in the galaxy. The gas velocities for [OIII] and H α emission lines show notable differences between narrow and broad components. For [OIII], narrow components have velocities of 163 ± 68 km s $^{-1}$ (north) and -208 ± 71 km s $^{-1}$ (south), while broad components show 132 ± 51 km s $^{-1}$ and -182 ± 28 km s $^{-1}$, respectively. For H α , the narrow components have velocities of 192 ± 34 km s $^{-1}$ (north) and -162 ± 42 km s $^{-1}$ (south), and broad components have 115 ± 47 km s $^{-1}$ and -129 ± 23 km s $^{-1}$. The higher values of velocity for narrow component compared to the broad component suggests that the narrow components is tracing the fast-moving gas in the galaxy. The residual velocity maps (Figure 7 (i) to (l)) shows that the narrow component exhibits a significant velocity offset from the stellar motion, and likely represents the outflowing gas influenced by the central AGN or jet. The measured average outflow velocities are 212 ± 33 km s $^{-1}$ for [O III] and 130 ± 18 km s $^{-1}$ for H α .
3. The outflow characteristics reveals that the [O III]-derived outflows are confined within 5 kpc, while H α -derived outflowing gas extends upto 10 kpc. The kinetic power for H α -derived outflows is 4.9×10^{41} ergs s $^{-1}$ and [O III]-derived outflows is 1.09×10^{41} ergs s $^{-1}$. Comparing the jet and the outflow energetics, we find that the radio jet is capable of driving the outflows. Furthermore, comparing the correlation between mass outflow rates, their energetics, and AGN bolometric luminosity with other similar samples in the literature, we find that NGC 5972 exhibits trends consistent with lower luminosity AGN.
4. The results from BPT analysis reveal that the gas along the jet axis is AGN ionized, whereas, the gas that is perpendicular to the jet is dominated by LINER-like emissions (Figure 9). This is consistent with results presented in Finlez et al. (2022). We have also performed MAPPINGS V shock modeling which shows that the best-fit model onto the AGN ionized region is shock+precursor whereas the region where we observe LINER-like

emissions shows pure shock ionization (see section 4.5). In section 5.2.1, we have argued that this transverse shock region could be an effect of jet-induced shock.

5. Based on our analysis, NGC 5972 has a kpc-scale radio jet with an estimated power of $P_{\text{jet}} \approx 10^{43}$ ergs s $^{-1}$, which aligns with the [O III] emission line region (Figure 7). Comparing this with other energy sources in the galaxy, we find that the jet power is higher than both the AGN kinetic power ($\approx 10^{42}$ ergs s $^{-1}$) and the mechanical power from star formation ($\approx 9.5 \times 10^{41}$ ergs s $^{-1}$). This indicates that the AGN-driven jet plays a significant role in the galaxy's energy dynamics.
6. The radio images of the galaxy reveal episodic activity, marked by surface brightness and spectral index discontinuities typical of double-double radio galaxies. Spectral age estimates, though uncertain, indicate the inner lobes are approximately 20 Myr old, while the outer lobes are around 40 Myr old, pointing to greater radiative losses in the outer lobes. Dynamical age estimates, based on typical FR II hotspot advance speeds, place the outer hotspots at 1.6-8 Myr and the inner hotspots at 35-170 Myr. The misalignment of the inner jets with the outer lobes suggests a merger event that shifted the jet axis. This scenario is supported by contrasting radio spectral indices, implying the inner jets are from a more recent AGN activity episode.

In summary, we propose a jet-driven feedback mechanism as an alternative explanation for the formation of the EELR in the Voorwerp galaxy, NGC 5972. Figure 14 shows a cartoon representation summarizing the proposed scenarios to explain the structures and alignment of the radio jet with the EELR. While we cannot completely dismiss the possibility of the faded Quasar model, the influence of the AGN jet effectively accounts for all the multi-wavelength properties and is a much simpler explanation.

ACKNOWLEDGEMENTS

We would like to thank Chetna Duggal for useful suggestions and discussions. PK acknowledges the support of the Department of Atomic Energy, Government of India, under the project 12-R&D-TFR-5.02-0700. SB, BS, and CO acknowledge support from the Natural Sciences and Engineering Research Council (NSERC) of Canada. SS acknowledges financial support from Millennium Nucleus NCN2023.002 (TITANs). O. Bait (OB) is supported by the *AstroSignals* Sinergia Project funded

by the Swiss National Science Foundation. This research has made use of the services of the ESO Science Archive Facility. The GALEX data presented in this paper were obtained from the Mikulski Archive for Space Telescopes (MAST) at the Space Telescope Science Institute. The specific observations analyzed can

be accessed via <http://dx.doi.org/10.17909/vpzv-2076> STScI is operated by the Association of Universities for Research in Astronomy, Inc., under NASA contract NAS5-26555. We thank the staff of the GMRT that made these observations possible. GMRT is run by the National Centre for Radio Astrophysics of the Tata Institute of Fundamental Research.

REFERENCES

- Alarie, A., & Morisset, C. 2019, *RMxAA*, 55, 377, doi: [10.22201/ia.01851101p.2019.55.02.21](https://doi.org/10.22201/ia.01851101p.2019.55.02.21)
- Bacon, R., Accardo, M., Adjali, L., et al. 2010, in *Society of Photo-Optical Instrumentation Engineers (SPIE) Conference Series*, Vol. 7735, *Ground-based and Airborne Instrumentation for Astronomy III*, ed. I. S. McLean, S. K. Ramsay, & H. Takami, 773508, doi: [10.1117/12.856027](https://doi.org/10.1117/12.856027)
- Baldwin, J. A., Phillips, M. M., & Terlevich, R. 1981, *PASP*, 93, 5, doi: [10.1086/130766](https://doi.org/10.1086/130766)
- Balmaverde, B., Capetti, A., Baldi, R. D., et al. 2022, *A&A*, 662, A23, doi: [10.1051/0004-6361/202142823](https://doi.org/10.1051/0004-6361/202142823)
- Baron, D., & Netzer, H. 2019, *MNRAS*, 486, 4290, doi: [10.1093/mnras/stz1070](https://doi.org/10.1093/mnras/stz1070)
- Baum, S. A., & Heckman, T. 1989, *ApJ*, 336, 681, doi: [10.1086/167043](https://doi.org/10.1086/167043)
- Baum, S. A., Heckman, T. M., Bridle, A., van Breugel, W. J. M., & Miley, G. K. 1988, *ApJS*, 68, 643, doi: [10.1086/191301](https://doi.org/10.1086/191301)
- Baum, S. A., O’Dea, C. P., Dallacassa, D., de Bruyn, A. G., & Pedlar, A. 1993, *ApJ*, 419, 553, doi: [10.1086/173508](https://doi.org/10.1086/173508)
- Bicknell, G. V., Dopita, M. A., Tsvetanov, Z. I., & Sutherland, R. S. 1998, *ApJ*, 495, 680, doi: [10.1086/305336](https://doi.org/10.1086/305336)
- Birzan, L., McNamara, B. R., Nulsen, P. E. J., Carilli, C. L., & Wise, M. W. 2008, *ApJ*, 686, 859, doi: [10.1086/591416](https://doi.org/10.1086/591416)
- Birzan, L., Rafferty, D. A., McNamara, B. R., Wise, M. W., & Nulsen, P. E. J. 2004, *ApJ*, 607, 800, doi: [10.1086/383519](https://doi.org/10.1086/383519)
- Bittner, A., Falcón-Barroso, J., Nedelchev, B., et al. 2019, *GIST: Galaxy IFU Spectroscopy Tool*, *Astrophysics Source Code Library*, record ascl:1907.025. <http://ascl.net/1907.025>
- Bridle, A. H., Hough, D. H., Lonsdale, C. J., Burns, J. O., & Laing, R. A. 1994, *AJ*, 108, 766, doi: [10.1086/117112](https://doi.org/10.1086/117112)
- Cappellari, M. 2017, *MNRAS*, 466, 798, doi: [10.1093/mnras/stw3020](https://doi.org/10.1093/mnras/stw3020)
- Cappellari, M., & Emsellem, E. 2004, *PASP*, 116, 138, doi: [10.1086/381875](https://doi.org/10.1086/381875)
- Carniani, S., Marconi, A., Maiolino, R., et al. 2015, *A&A*, 580, A102, doi: [10.1051/0004-6361/201526557](https://doi.org/10.1051/0004-6361/201526557)
- Cavagnolo, K. W., McNamara, B. R., Nulsen, P. E. J., et al. 2010, *ApJ*, 720, 1066, doi: [10.1088/0004-637X/720/2/1066](https://doi.org/10.1088/0004-637X/720/2/1066)
- Cazzoli, S., Hermosa Muñoz, L., Márquez, I., et al. 2022, *A&A*, 664, A135, doi: [10.1051/0004-6361/202142695](https://doi.org/10.1051/0004-6361/202142695)
- Chojnowski, D., & Keel, W. C. 2011, in *American Astronomical Society Meeting Abstracts*, Vol. 217, *American Astronomical Society Meeting Abstracts #217*, 142.07
- Cid Fernandes, R., Stasińska, G., Mateus, A., & Vale Asari, N. 2011, *MNRAS*, 413, 1687, doi: [10.1111/j.1365-2966.2011.18244.x](https://doi.org/10.1111/j.1365-2966.2011.18244.x)
- Colbert, E. J. M., Baum, S. A., Gallimore, J. F., O’Dea, C. P., & Christensen, J. A. 1996, *ApJ*, 467, 551, doi: [10.1086/177633](https://doi.org/10.1086/177633)
- Condon, J. J. 1992, *ARA&A*, 30, 575, doi: [10.1146/annurev.aa.30.090192.003043](https://doi.org/10.1146/annurev.aa.30.090192.003043)
- Condon, J. J., & Ransom, S. M. 2016, *Essential Radio Astronomy*
- Couto, G. S., Storchi-Bergmann, T., Axon, D. J., et al. 2013, *MNRAS*, 435, 2982, doi: [10.1093/mnras/stt1491](https://doi.org/10.1093/mnras/stt1491)
- Couto, G. S., Storchi-Bergmann, T., & Schnorr-Müller, A. 2017, *MNRAS*, 469, 1573, doi: [10.1093/mnras/stx962](https://doi.org/10.1093/mnras/stx962)
- Crain, R. A., Schaye, J., Bower, R. G., et al. 2015, *MNRAS*, 450, 1937, doi: [10.1093/mnras/stv725](https://doi.org/10.1093/mnras/stv725)
- Dannen, R. C., Proga, D., Waters, T., & Dyda, S. 2020, *ApJL*, 893, L34, doi: [10.3847/2041-8213/ab87a5](https://doi.org/10.3847/2041-8213/ab87a5)
- Davé, R., Anglés-Alcázar, D., Narayanan, D., et al. 2019, *MNRAS*, 486, 2827, doi: [10.1093/mnras/stz937](https://doi.org/10.1093/mnras/stz937)
- Davidson, K., & Netzer, H. 1979, *Reviews of Modern Physics*, 51, 715, doi: [10.1103/RevModPhys.51.715](https://doi.org/10.1103/RevModPhys.51.715)
- de Bruyn, A. G., & Wilson, A. S. 1978a, *A&A*, 64, 433
- . 1978b, *A&A*, 64, 433
- Di Matteo, T., Springel, V., & Hernquist, L. 2005, *Nature*, 433, 604, doi: [10.1038/nature03335](https://doi.org/10.1038/nature03335)
- Dimitrijević, M. S., Popović, L. Č., Kovačević, J., Dačić, M., & Ilić, D. 2007, *MNRAS*, 374, 1181, doi: [10.1111/j.1365-2966.2006.11238.x](https://doi.org/10.1111/j.1365-2966.2006.11238.x)

- Dopita, M. A., & Sutherland, R. S. 1995, *ApJ*, 455, 468, doi: [10.1086/176596](https://doi.org/10.1086/176596)
- Dubois, Y., Beckmann, R., Bournaud, F., et al. 2021, *A&A*, 651, A109, doi: [10.1051/0004-6361/202039429](https://doi.org/10.1051/0004-6361/202039429)
- Duggal, C., O’Dea, C., Baum, S., et al. 2021, *Astronomische Nachrichten*, 342, 1087, doi: [10.1002/asna.20210054](https://doi.org/10.1002/asna.20210054)
- Duggal, C., O’Dea, C., Baum, S., et al. 2023, in *American Astronomical Society Meeting Abstracts*, Vol. 241, American Astronomical Society Meeting Abstracts, 336.01
- Emonts, B. H. C., Morganti, R., Tadhunter, C. N., et al. 2005, *MNRAS*, 362, 931, doi: [10.1111/j.1365-2966.2005.09354.x](https://doi.org/10.1111/j.1365-2966.2005.09354.x)
- Fabian, A. C. 1999, *MNRAS*, 308, L39, doi: [10.1046/j.1365-8711.1999.03017.x](https://doi.org/10.1046/j.1365-8711.1999.03017.x)
- Falcón-Barroso, J., Bacon, R., Bureau, M., et al. 2006, *MNRAS*, 369, 529, doi: [10.1111/j.1365-2966.2006.10261.x](https://doi.org/10.1111/j.1365-2966.2006.10261.x)
- Faucher-Giguère, C.-A., & Quataert, E. 2012, *MNRAS*, 425, 605, doi: [10.1111/j.1365-2966.2012.21512.x](https://doi.org/10.1111/j.1365-2966.2012.21512.x)
- Ferland, G. J., & Netzer, H. 1983, *ApJ*, 264, 105, doi: [10.1086/160577](https://doi.org/10.1086/160577)
- Finlez, C., Nagar, N. M., Storchi-Bergmann, T., et al. 2018, *MNRAS*, 479, 3892, doi: [10.1093/mnras/sty1555](https://doi.org/10.1093/mnras/sty1555)
- Finlez, C., Treister, E., Bauer, F., et al. 2022, *ApJ*, 936, 88, doi: [10.3847/1538-4357/ac854e](https://doi.org/10.3847/1538-4357/ac854e)
- Fiore, F., Feruglio, C., Shankar, F., et al. 2017, *A&A*, 601, A143, doi: [10.1051/0004-6361/201629478](https://doi.org/10.1051/0004-6361/201629478)
- Gaibler, V., Khochfar, S., Krause, M., & Silk, J. 2012, *MNRAS*, 425, 438, doi: [10.1111/j.1365-2966.2012.21479.x](https://doi.org/10.1111/j.1365-2966.2012.21479.x)
- Gallimore, J. F., Axon, D. J., O’Dea, C. P., Baum, S. A., & Pedlar, A. 2006, *AJ*, 132, 546, doi: [10.1086/504593](https://doi.org/10.1086/504593)
- Garrington, S. T., Leahy, J. P., Conway, R. G., & Laing, R. A. 1988, *Nature*, 331, 147, doi: [10.1038/331147a0](https://doi.org/10.1038/331147a0)
- Girdhar, A. 2022, in *Hypatia Colloquium 2022*, 2, doi: [10.5281/zenodo.7104492](https://doi.org/10.5281/zenodo.7104492)
- Harrison, C. M., Alexander, D. M., Mullaney, J. R., & Swinbank, A. M. 2014, *MNRAS*, 441, 3306, doi: [10.1093/mnras/stu515](https://doi.org/10.1093/mnras/stu515)
- Harrison, C. M., Costa, T., Tadhunter, C. N., et al. 2018, *Nature Astronomy*, 2, 198, doi: [10.1038/s41550-018-0403-6](https://doi.org/10.1038/s41550-018-0403-6)
- Harrison, C. M., Thomson, A. P., Alexander, D. M., et al. 2015, *ApJ*, 800, 45, doi: [10.1088/0004-637X/800/1/45](https://doi.org/10.1088/0004-637X/800/1/45)
- Harvey, T., Maksym, W. P., Keel, W., et al. 2022, arXiv e-prints, arXiv:2208.05915. <https://arxiv.org/abs/2208.05915>
- Helou, G., Khan, I. R., Malek, L., & Boehmer, L. 1988, *ApJS*, 68, 151, doi: [10.1086/191285](https://doi.org/10.1086/191285)
- Holt, J., Tadhunter, C. N., & Morganti, R. 2008, *MNRAS*, 387, 639, doi: [10.1111/j.1365-2966.2008.13089.x](https://doi.org/10.1111/j.1365-2966.2008.13089.x)
- Ishibashi, W., & Courvoisier, T. J. L. 2011, *A&A*, 525, A118, doi: [10.1051/0004-6361/201014987](https://doi.org/10.1051/0004-6361/201014987)
- Ishibashi, W., Fabian, A. C., & Canning, R. E. A. 2013, *MNRAS*, 431, 2350, doi: [10.1093/mnras/stt333](https://doi.org/10.1093/mnras/stt333)
- Jarvis, M. E., Harrison, C. M., Thomson, A. P., et al. 2019, *MNRAS*, 485, 2710, doi: [10.1093/mnras/stz556](https://doi.org/10.1093/mnras/stz556)
- Jarvis, M. E., Harrison, C. M., Mainieri, V., et al. 2021, *MNRAS*, 503, 1780, doi: [10.1093/mnras/stab549](https://doi.org/10.1093/mnras/stab549)
- Jiang, Y.-F., Ciotti, L., Ostriker, J. P., & Spitkovsky, A. 2010, *ApJ*, 711, 125, doi: [10.1088/0004-637X/711/1/125](https://doi.org/10.1088/0004-637X/711/1/125)
- Józsa, G. I. G., Garrett, M. A., Oosterloo, T. A., et al. 2009, *A&A*, 500, L33, doi: [10.1051/0004-6361/200912402](https://doi.org/10.1051/0004-6361/200912402)
- Kaasinen, M., Bian, F., Groves, B., Kewley, L. J., & Gupta, A. 2017, *MNRAS*, 465, 3220, doi: [10.1093/mnras/stw2827](https://doi.org/10.1093/mnras/stw2827)
- Kakkad, D., Groves, B., Dopita, M., et al. 2018, *A&A*, 618, A6, doi: [10.1051/0004-6361/201832790](https://doi.org/10.1051/0004-6361/201832790)
- Kakkad, D., Sani, E., Rojas, A. F., et al. 2022, *MNRAS*, 511, 2105, doi: [10.1093/mnras/stac103](https://doi.org/10.1093/mnras/stac103)
- Kauffmann, G., Heckman, T. M., Tremonti, C., et al. 2003, *MNRAS*, 346, 1055, doi: [10.1111/j.1365-2966.2003.07154.x](https://doi.org/10.1111/j.1365-2966.2003.07154.x)
- Kaviraj, S., Laigle, C., Kimm, T., et al. 2017, *MNRAS*, 467, 4739, doi: [10.1093/mnras/stx126](https://doi.org/10.1093/mnras/stx126)
- Keel, W. C., Lintott, C., Schawinski, K., et al. 2011, in *American Astronomical Society Meeting Abstracts*, Vol. 217, American Astronomical Society Meeting Abstracts #217, 142.08
- Keel, W. C., Lintott, C. J., Schawinski, K., et al. 2012a, *AJ*, 144, 66, doi: [10.1088/0004-6256/144/2/66](https://doi.org/10.1088/0004-6256/144/2/66)
- Keel, W. C., Chojnowski, S. D., Bennert, V. N., et al. 2012b, *MNRAS*, 420, 878, doi: [10.1111/j.1365-2966.2011.20101.x](https://doi.org/10.1111/j.1365-2966.2011.20101.x)
- Keel, W. C., Maksym, W. P., Bennert, V. N., et al. 2015, *AJ*, 149, 155, doi: [10.1088/0004-6256/149/5/155](https://doi.org/10.1088/0004-6256/149/5/155)
- Keel, W. C., Lintott, C. J., Maksym, W. P., et al. 2017, *ApJ*, 835, 256, doi: [10.3847/1538-4357/835/2/256](https://doi.org/10.3847/1538-4357/835/2/256)
- Kellermann, K. I., Sramek, R., Schmidt, M., Shaffer, D. B., & Green, R. 1989, *AJ*, 98, 1195, doi: [10.1086/115207](https://doi.org/10.1086/115207)
- Kennicutt, Robert C., J. 1998, *ARA&A*, 36, 189, doi: [10.1146/annurev.astro.36.1.189](https://doi.org/10.1146/annurev.astro.36.1.189)
- Kewley, L. J., Dopita, M. A., Sutherland, R. S., Heisler, C. A., & Trevena, J. 2001, *ApJ*, 556, 121, doi: [10.1086/321545](https://doi.org/10.1086/321545)
- Kharb, P., O’Dea, C. P., Baum, S. A., Colbert, E. J. M., & Xu, C. 2006, *ApJ*, 652, 177, doi: [10.1086/507945](https://doi.org/10.1086/507945)
- Kharb, P., Srivastava, S., Singh, V., et al. 2016, *MNRAS*, 459, 1310, doi: [10.1093/mnras/stw699](https://doi.org/10.1093/mnras/stw699)
- Kozlova, D. V., Moiseev, A. V., & Smirnova, A. A. 2020, *Contributions of the Astronomical Observatory Skalnaté Pleso*, 50, 309, doi: [10.31577/caosp.2020.50.1.309](https://doi.org/10.31577/caosp.2020.50.1.309)

- Krolik, J. H., & Vrtilik, J. M. 1984, *ApJ*, 279, 521, doi: [10.1086/161916](https://doi.org/10.1086/161916)
- Kumar, N., & Mukhopadhyay, B. 2021, arXiv e-prints, arXiv:2106.06267, doi: [10.48550/arXiv.2106.06267](https://doi.org/10.48550/arXiv.2106.06267)
- Laing, R. A. 1988, *Nature*, 331, 149, doi: [10.1038/331149a0](https://doi.org/10.1038/331149a0)
- Lanz, L., Ogle, P. M., Evans, D., et al. 2015, *ApJ*, 801, 17, doi: [10.1088/0004-637X/801/1/17](https://doi.org/10.1088/0004-637X/801/1/17)
- Lena, D., Robinson, A., Storchi-Bergman, T., et al. 2015, *ApJ*, 806, 84, doi: [10.1088/0004-637X/806/1/84](https://doi.org/10.1088/0004-637X/806/1/84)
- Lintott, C. J., Schawinski, K., Keel, W., et al. 2009, *MNRAS*, 399, 129, doi: [10.1111/j.1365-2966.2009.15299.x](https://doi.org/10.1111/j.1365-2966.2009.15299.x)
- Mahony, E. K., Oonk, J. B. R., Morganti, R., et al. 2016, *MNRAS*, 455, 2453, doi: [10.1093/mnras/stv2456](https://doi.org/10.1093/mnras/stv2456)
- Marecki, A., Jamrozy, M., & Machalski, J. 2016, *MNRAS*, 463, 338, doi: [10.1093/mnras/stw2006](https://doi.org/10.1093/mnras/stw2006)
- Marecki, A., Jamrozy, M., Machalski, J., & Pajdosz-Śmierciak, U. 2021, *MNRAS*, 501, 853, doi: [10.1093/mnras/staa3632](https://doi.org/10.1093/mnras/staa3632)
- Marecki, A., Sebastian, B., & Ishwara-Chandra, C. H. 2023, *MNRAS*, 518, L83, doi: [10.1093/mnrasl/slac105](https://doi.org/10.1093/mnrasl/slac105)
- McCarthy, P. J., Spinrad, H., & van Breugel, W. 1995, *ApJS*, 99, 27, doi: [10.1086/192178](https://doi.org/10.1086/192178)
- Merloni, A., & Heinz, S. 2007, *MNRAS*, 381, 589, doi: [10.1111/j.1365-2966.2007.12253.x](https://doi.org/10.1111/j.1365-2966.2007.12253.x)
- Merritt, D., & Ekers, R. D. 2002, *Science*, 297, 1310, doi: [10.1126/science.1074688](https://doi.org/10.1126/science.1074688)
- Mingozzi, M., Cresci, G., Venturi, G., et al. 2019, *A&A*, 622, A146, doi: [10.1051/0004-6361/201834372](https://doi.org/10.1051/0004-6361/201834372)
- Molina, M., Eracleous, M., Barth, A. J., et al. 2018, *ApJ*, 864, 90, doi: [10.3847/1538-4357/aad5ed](https://doi.org/10.3847/1538-4357/aad5ed)
- Morganti, R., Oosterloo, T., Oonk, J. B. R., Frieswijk, W., & Tadhunter, C. 2015, *A&A*, 580, A1, doi: [10.1051/0004-6361/201525860](https://doi.org/10.1051/0004-6361/201525860)
- Morganti, R., Veilleux, S., Oosterloo, T., Teng, S. H., & Rupke, D. 2016, *A&A*, 593, A30, doi: [10.1051/0004-6361/201628978](https://doi.org/10.1051/0004-6361/201628978)
- Mullaney, J. R., Alexander, D. M., Fine, S., et al. 2013, *MNRAS*, 433, 622, doi: [10.1093/mnras/stt751](https://doi.org/10.1093/mnras/stt751)
- Murray, N., Quataert, E., & Thompson, T. A. 2005, *ApJ*, 618, 569, doi: [10.1086/426067](https://doi.org/10.1086/426067)
- Nandi, S., Saikia, D. J., Roy, R., et al. 2019, *MNRAS*, 486, 5158, doi: [10.1093/mnras/stz1184](https://doi.org/10.1093/mnras/stz1184)
- Napier, P. J., Thompson, A. R., & Ekers, R. D. 1983, *IEEE Proceedings*, 71, 1295
- Nelson, C. H., & Whittle, M. 1996, *ApJ*, 465, 96, doi: [10.1086/177405](https://doi.org/10.1086/177405)
- Nelson, D., Kauffmann, G., Pillepich, A., et al. 2018, *MNRAS*, 477, 450, doi: [10.1093/mnras/sty656](https://doi.org/10.1093/mnras/sty656)
- Nesvadba, N. P. H., De Breuck, C., Lehnert, M. D., Best, P. N., & Collet, C. 2017a, *A&A*, 599, A123, doi: [10.1051/0004-6361/201528040](https://doi.org/10.1051/0004-6361/201528040)
- Nesvadba, N. P. H., Drouart, G., De Breuck, C., et al. 2017b, *A&A*, 600, A121, doi: [10.1051/0004-6361/201629357](https://doi.org/10.1051/0004-6361/201629357)
- Nims, J., Quataert, E., & Faucher-Giguère, C.-A. 2015, *MNRAS*, 447, 3612, doi: [10.1093/mnras/stu2648](https://doi.org/10.1093/mnras/stu2648)
- O'Dea, C. P., Daly, R. A., Kharb, P., Freeman, K. A., & Baum, S. A. 2009, *A&A*, 494, 471, doi: [10.1051/0004-6361:200809416](https://doi.org/10.1051/0004-6361:200809416)
- O'Dea, C. P., & Owen, F. N. 1987, *ApJ*, 316, 95, doi: [10.1086/165182](https://doi.org/10.1086/165182)
- Osterbrock, D. E., & Ferland, G. J. 2006, *Astrophysics of gaseous nebulae and active galactic nuclei*
- Pérez-Torres, M. A., & Alberdi, A. 2007, *MNRAS*, 379, 275, doi: [10.1111/j.1365-2966.2007.11944.x](https://doi.org/10.1111/j.1365-2966.2007.11944.x)
- Perley, R. A., Chandler, C. J., Butler, B. J., & Wrobel, J. M. 2011, *ApJL*, 739, L1, doi: [10.1088/2041-8205/739/1/L1](https://doi.org/10.1088/2041-8205/739/1/L1)
- Perna, M., Arribas, S., Catalán-Torrecilla, C., et al. 2020, *A&A*, 643, A139, doi: [10.1051/0004-6361/202038328](https://doi.org/10.1051/0004-6361/202038328)
- Pillepich, A., Springel, V., Nelson, D., et al. 2018, *MNRAS*, 473, 4077, doi: [10.1093/mnras/stx2656](https://doi.org/10.1093/mnras/stx2656)
- Rao, V. V., Kharb, P., Rubinur, K., et al. 2023, *MNRAS*, 524, 1615, doi: [10.1093/mnras/stad1901](https://doi.org/10.1093/mnras/stad1901)
- Rau, U., & Cornwell, T. J. 2011, *A&A*, 532, A71, doi: [10.1051/0004-6361/201117104](https://doi.org/10.1051/0004-6361/201117104)
- Rosario, D. J., Burtscher, L., Davies, R., et al. 2013, *ApJ*, 778, 94, doi: [10.1088/0004-637X/778/2/94](https://doi.org/10.1088/0004-637X/778/2/94)
- Rose, M., Tadhunter, C., Ramos Almeida, C., et al. 2018, *MNRAS*, 474, 128, doi: [10.1093/mnras/stx2590](https://doi.org/10.1093/mnras/stx2590)
- Rubinur, K., Das, M., Kharb, P., & Honey, M. 2017, *MNRAS*, 465, 4772, doi: [10.1093/mnras/stw2981](https://doi.org/10.1093/mnras/stw2981)
- Ruschel-Dutra, D., Storchi-Bergmann, T., Schnorr-Müller, A., et al. 2021, *MNRAS*, 507, 74, doi: [10.1093/mnras/stab2058](https://doi.org/10.1093/mnras/stab2058)
- Sambruna, R. M., Netzer, H., Kaspi, S., et al. 2001, *ApJL*, 546, L13, doi: [10.1086/318068](https://doi.org/10.1086/318068)
- Sanders, R. L., Shapley, A. E., Kriek, M., et al. 2016, *ApJ*, 816, 23, doi: [10.3847/0004-637X/816/1/23](https://doi.org/10.3847/0004-637X/816/1/23)
- Sartori, L. F., Schawinski, K., Koss, M., et al. 2016, *MNRAS*, 457, 3629, doi: [10.1093/mnras/stw230](https://doi.org/10.1093/mnras/stw230)
- Sarzi, M., Falcón-Barroso, J., Davies, R. L., et al. 2006, *MNRAS*, 366, 1151, doi: [10.1111/j.1365-2966.2005.09839.x](https://doi.org/10.1111/j.1365-2966.2005.09839.x)
- Schawinski, K., Thomas, D., Sarzi, M., et al. 2007, *MNRAS*, 382, 1415, doi: [10.1111/j.1365-2966.2007.12487.x](https://doi.org/10.1111/j.1365-2966.2007.12487.x)
- Schawinski, K., Evans, D. A., Virani, S., et al. 2010, *ApJL*, 724, L30, doi: [10.1088/2041-8205/724/1/L30](https://doi.org/10.1088/2041-8205/724/1/L30)

- Schaye, J., & Dalla Vecchia, C. 2008, *MNRAS*, 383, 1210, doi: [10.1111/j.1365-2966.2007.12639.x](https://doi.org/10.1111/j.1365-2966.2007.12639.x)
- Schaye, J., Crain, R. A., Bower, R. G., et al. 2015, *MNRAS*, 446, 521, doi: [10.1093/mnras/stu2058](https://doi.org/10.1093/mnras/stu2058)
- Schiano, A. V. R. 1986, *ApJ*, 302, 81, doi: [10.1086/163975](https://doi.org/10.1086/163975)
- Schmitt, H. R., Donley, J. L., Antonucci, R. R. J., et al. 2003, *ApJ*, 597, 768, doi: [10.1086/381224](https://doi.org/10.1086/381224)
- Sebastian, B., Ishwara-Chandra, C. H., Joshi, R., & Wadadekar, Y. 2018, *MNRAS*, 473, 4926, doi: [10.1093/mnras/stx2631](https://doi.org/10.1093/mnras/stx2631)
- Sebastian, B., Kharb, P., O’Dea, C. P., Colbert, E. J. M., & Baum, S. A. 2019a, *ApJ*, 883, 189, doi: [10.3847/1538-4357/ab371a](https://doi.org/10.3847/1538-4357/ab371a)
- Sebastian, B., Kharb, P., O’Dea, C. P., Gallimore, J. F., & Baum, S. A. 2019b, *MNRAS*, 490, L26, doi: [10.1093/mnrasl/slz136](https://doi.org/10.1093/mnrasl/slz136)
- . 2020, *MNRAS*, 499, 334, doi: [10.1093/mnras/staa2473](https://doi.org/10.1093/mnras/staa2473)
- Sebastian, B., Caproni, A., Kharb, P., et al. 2024, *MNRAS*, 530, 4902, doi: [10.1093/mnras/stae546](https://doi.org/10.1093/mnras/stae546)
- Shih, H.-Y., & Stockton, A. 2014, *ApJ*, 786, 3, doi: [10.1088/0004-637X/786/1/3](https://doi.org/10.1088/0004-637X/786/1/3)
- Silpa, S., Kharb, P., Harrison, C. M., et al. 2022, *MNRAS*, 513, 4208, doi: [10.1093/mnras/stac1044](https://doi.org/10.1093/mnras/stac1044)
- Singh, R., van de Ven, G., Jahnke, K., et al. 2013, *A&A*, 558, A43, doi: [10.1051/0004-6361/201322062](https://doi.org/10.1051/0004-6361/201322062)
- Singha, M., O’Dea, C. P., & Baum, S. A. 2023, *Galaxies*, 11, 85, doi: [10.3390/galaxies11040085](https://doi.org/10.3390/galaxies11040085)
- Singha, M., Husemann, B., Urrutia, T., et al. 2022, *A&A*, 659, A123, doi: [10.1051/0004-6361/202040122](https://doi.org/10.1051/0004-6361/202040122)
- Smith, D. J. B., Krause, M. G., Hardcastle, M. J., & Drake, A. B. 2022, *MNRAS*, 514, 3879, doi: [10.1093/mnras/stac1568](https://doi.org/10.1093/mnras/stac1568)
- Spoon, H. W. W., & Holt, J. 2009, *ApJL*, 702, L42, doi: [10.1088/0004-637X/702/1/L42](https://doi.org/10.1088/0004-637X/702/1/L42)
- Springel, V., Pakmor, R., Pillepich, A., et al. 2018, *MNRAS*, 475, 676, doi: [10.1093/mnras/stx3304](https://doi.org/10.1093/mnras/stx3304)
- Steiman-Cameron, T. Y., Kormendy, J., & Durisen, R. H. 1992, *AJ*, 104, 1339, doi: [10.1086/116323](https://doi.org/10.1086/116323)
- Stocke, J. T., Morris, S. L., Weymann, R. J., & Foltz, C. B. 1992, *ApJ*, 396, 487, doi: [10.1086/171735](https://doi.org/10.1086/171735)
- Storey, P. J., & Zeppen, C. J. 2000, *MNRAS*, 312, 813, doi: [10.1046/j.1365-8711.2000.03184.x](https://doi.org/10.1046/j.1365-8711.2000.03184.x)
- Sutherland, R., Dopita, M., Binette, L., & Groves, B. 2018, *MAPPINGS V: Astrophysical plasma modeling code*, Astrophysics Source Code Library, record ascl:1807.005
- Sutherland, R. S., & Bicknell, G. V. 2007, *ApJS*, 173, 37, doi: [10.1086/520640](https://doi.org/10.1086/520640)
- Tadhunter, C. N., Fosbury, R. A. E., & Quinn, P. J. 1989, *MNRAS*, 240, 225, doi: [10.1093/mnras/240.2.225](https://doi.org/10.1093/mnras/240.2.225)
- Thompson, T. A., Fabian, A. C., Quataert, E., & Murray, N. 2015, *MNRAS*, 449, 147, doi: [10.1093/mnras/stv246](https://doi.org/10.1093/mnras/stv246)
- Vazdekis, A., Coelho, P., Cassisi, S., et al. 2015, *MNRAS*, 449, 1177, doi: [10.1093/mnras/stv151](https://doi.org/10.1093/mnras/stv151)
- Veilleux, S. 1991, *ApJ*, 369, 331, doi: [10.1086/169765](https://doi.org/10.1086/169765)
- Veilleux, S., & Osterbrock, D. E. 1987, *ApJS*, 63, 295, doi: [10.1086/191166](https://doi.org/10.1086/191166)
- Venturi, G., Cresci, G., Marconi, A., et al. 2021, *A&A*, 648, A17, doi: [10.1051/0004-6361/202039869](https://doi.org/10.1051/0004-6361/202039869)
- Venturi, G., Treister, E., Finlez, C., et al. 2023a, *A&A*, 678, A127, doi: [10.1051/0004-6361/202347375](https://doi.org/10.1051/0004-6361/202347375)
- . 2023b, arXiv e-prints, arXiv:2309.02498, doi: [10.48550/arXiv.2309.02498](https://doi.org/10.48550/arXiv.2309.02498)
- Veron, P., & Veron-Cetty, M. P. 1995, *A&A*, 296, 315
- Villar-Martín, M., Emonts, B., Cabrera Lavers, A., et al. 2017, *MNRAS*, 472, 4659, doi: [10.1093/mnras/stx2209](https://doi.org/10.1093/mnras/stx2209)
- Virtanen, P., Gommers, R., Oliphant, T. E., et al. 2020, *Nature Methods*, 17, 261, doi: [10.1038/s41592-019-0686-2](https://doi.org/10.1038/s41592-019-0686-2)
- Vogelsberger, M., Marinacci, F., Torrey, P., et al. 2018, *MNRAS*, 474, 2073, doi: [10.1093/mnras/stx2955](https://doi.org/10.1093/mnras/stx2955)
- Wagner, A. Y., & Bicknell, G. V. 2011, *ApJ*, 728, 29, doi: [10.1088/0004-637X/728/1/29](https://doi.org/10.1088/0004-637X/728/1/29)
- Wagner, A. Y., Bicknell, G. V., & Umemura, M. 2012, *ApJ*, 757, 136, doi: [10.1088/0004-637X/757/2/136](https://doi.org/10.1088/0004-637X/757/2/136)
- Wang, J.-M. 2008, *ApJL*, 682, L81, doi: [10.1086/590928](https://doi.org/10.1086/590928)
- Whittle, M., & Wilson, A. S. 2004, *AJ*, 127, 606, doi: [10.1086/380940](https://doi.org/10.1086/380940)
- Zakamska, N. L., & Greene, J. E. 2014, *MNRAS*, 442, 784, doi: [10.1093/mnras/stu842](https://doi.org/10.1093/mnras/stu842)
- Zubovas, K., & King, A. 2012, *ApJL*, 745, L34, doi: [10.1088/2041-8205/745/2/L34](https://doi.org/10.1088/2041-8205/745/2/L34)